

Manuscript Number: LITHOS8788R3

Title: Origin of magmatic harzburgite as a result of boninite magma evolution - An illustration using layered harzburgite-dunite cumulate from the Troodos ophiolite complex

Article Type: Regular Article

Keywords: cumulate harzburgite; petrogenesis; boninite magma evolution; Troodos ophiolite; fractional crystallization

Corresponding Author: Miss Fangyu Shen,

Corresponding Author's Institution: Institute of Oceanology, Chinese Academy of Sciences

First Author: Fangyu Shen

Order of Authors: Fangyu Shen; Yaoling Niu; Yanhong Chen; Yajie Gao; Xiaohong Wang; Meng Duan; Li Shan

Abstract: Olivine (Ol) and orthopyroxene (Opx) are the primary liquidus phases of boninite in modern subduction settings and in many ophiolite complexes. It is thus straightforward to expect the formation of harzburgite cumulate resulting from boninite magma evolution. However, such magmatic harzburgite has been rarely studied. Here, we report the results of our study on such harzburgite from the Troodos ophiolite complex.

The Troodos cumulate harzburgite (locally lherzolite) is characteristically interlayered with dunite, showing varying thickness on millimeter to decimeter scales, as the result of volumetrically varying multiple pulses of melt injection into the evolving magma chamber. We illustrate the development of the interlayered cumulate by phase equilibrium analysis. The parental melt of each pulse begins to crystallize olivine to form a dunite layer before reaching the Ol-Opx cotectic, along which Ol and Opx coprecipitate to form a harzburgite layer. Periodical replenishment will result in dunite-harzburgite interlayered cumulate. In cases when replenishment may be delayed, the melt along the Ol-Opx cotectic can evolve to the Ol-Opx-clinopyroxene (Cpx) eutectic to form harzburgite with some Cpx or lherzolite. The calculated melts in equilibrium with spinels in the cumulate are characteristic of boninite in major element compositional spaces. The calculated melts in equilibrium with Cpx and Opx in the cumulate share the same as, or identical to, trace element patterns of the Troodos boninite (both glasses and bulk-rock compositions). Petrological modeling of the boninite magma evolution shows a crystallization order of Ol, Opx, Cpx, plagioclase. Our study also emphasizes the importance in considering dunite-harzburgite/lherzolite cumulate when interpreting seismic structure of the crust in subduction settings, especially in rock sequences associated with subduction initiation thought to be indicated by boninite magmatism.

Research Data Related to this Submission

Title: Data for: Origin of magmatic harzburgite as a result of boninite
magma evolution - An illustration using layered harzburgite-dunite
cumulate from the Troodos ophiolite complex

Repository: Mendeley Data

<https://data.mendeley.com/datasets/44k3x7fwcm/draft?a=608adf26-06ef-43d6-99ca-a4db2caf9340>

- The magmatic harzburgite in Troodos results from boninite magma evolution.
- The melts in equilibrium with minerals in the cumulate are similar to boninite.
- Petrological modeling shows the crystallization order of boninite evolution.
- Crystallization of periodically replenished boninite melts produces the cumulate.

1 **Origin of magmatic harzburgite as a result of boninite magma**
2 **evolution – An illustration using layered harzburgite-dunite cumulate**
3 **from the Troodos ophiolite complex**

4

5 Fangyu Shen ^{a,b,c,d,*}, Yaoling Niu ^{a,b,c,e,*}, Yanhong Chen ^{b,e}, Yajie Gao ^f, Xiaohong
6 Wang ^{a,c}, Meng Duan ^{a,c}, Li Shan ^{a,c,d}

7 ^a *Institute of Oceanology, Chinese Academy of Sciences, Qingdao 266071, China*

8 ^b *Department of Earth Sciences, Durham University, Durham DH1 3LE, UK*

9 ^c *Laboratory for Marine Geology, Qingdao National Laboratory for Marine Science and*
10 *Technology, Qingdao 266061, China*

11 ^d *University of Chinese Academy of Sciences, Beijing 100049, China*

12 ^e *School of Earth Sciences and Resources, China University of Geosciences, Beijing 100083, China*

13 ^f *Research School of Earth Sciences, Australian National University, Canberra, ACT 2601,*
14 *Australia*

15 * Corresponding authors at: Institute of Oceanology, Chinese Academy of Sciences, Qingdao
16 266071, China.

17 E-mail addresses: fangyushen@qdio.ac.cn (F. Shen), yaoling.niu@durham.ac.uk (Y. Niu).

18

19 **Keywords:**

20 Cumulate harzburgite

21 Petrogenesis

22 Boninite magma evolution

23 Troodos ophiolite

24 Fractional crystallization

25 **Abstract**

26 Olivine (Ol) and orthopyroxene (Opx) are the primary liquidus phases of boninite in
27 modern subduction settings and in many ophiolite complexes. It is thus
28 straightforward to expect the formation of harzburgite cumulate resulting from
29 boninite magma evolution. However, such magmatic harzburgite has been rarely
30 studied. Here, we report the results of our study on such harzburgite from the Troodos
31 ophiolite complex.

32 The Troodos cumulate harzburgite (locally lherzolite) is characteristically
33 interlayered with dunite, showing varying thickness on millimeter to decimeter scales,
34 as the result of volumetrically varying multiple pulses of melt injection into the
35 evolving magma chamber. We illustrate the development of the interlayered cumulate
36 by phase equilibrium analysis. The parental melt of each pulse begins to crystallize
37 olivine to form a dunite layer before reaching the Ol-Opx cotectic, along which Ol
38 and Opx coprecipitate to form a harzburgite layer. Periodical replenishment will result
39 in dunite-harzburgite interlayered cumulate. In cases when replenishment may be
40 delayed, the melt along the Ol-Opx cotectic can evolve to the Ol-Opx-clinopyroxene
41 (Cpx) eutectic to form harzburgite with some Cpx or lherzolite. The calculated melts
42 in equilibrium with spinels in the cumulate are characteristic of boninite in major
43 element compositional spaces. The calculated melts in equilibrium with Cpx and Opx
44 in the cumulate share the same as, or identical to, trace element patterns of the
45 Troodos boninite (both glasses and bulk-rock compositions). Petrological modeling of
46 the boninite magma evolution shows a crystallization order of Ol, Opx, Cpx,

47 plagioclase. Our study also emphasizes the importance in considering
48 dunite-harzburgite/lherzolite cumulate when interpreting seismic structure of the crust
49 in subduction settings, especially in rock sequences associated with subduction
50 initiation thought to be indicated by boninite magmatism.

51 **1 Introduction**

52 Harzburgite, dominated by olivine (Ol) and orthopyroxene (Opx), as mantle
53 melting residue has been well understood (e.g., [Jaques and Green, 1980](#); [Dick et al.,](#)
54 [1984](#); [Niu, 1997, 2004](#)), and as a cumulate constituent in layered intrusions has also
55 been well studied (e.g., [Cawthorn, 1996](#); [Charlier et al., 2015](#)). Because Ol and Opx
56 are the primary liquidus phases of boninite in modern subduction settings and in many
57 ophiolite complexes, it is expected that the boninite magma evolution will produce
58 cumulate harzburgite. However, cumulate harzburgite as the result of boninite magma
59 evolution has not been well documented and investigated. The cumulate harzburgite
60 reported in layered intrusions was mostly ascribed to crystal settling or magma mixing
61 in the magma chamber (e.g., [Irvine and Smith, 1967](#); [Raedeke and McCallam, 1984](#)).
62 On the basis of previous works and many years of our careful field observations, we
63 have hypothesized that the ultramafic rock suites interlayered between dunite and
64 harzburgite (locally lherzolite) in the Troodos Ophiolite complex must represent
65 cumulate as the result of fractional crystallization of boninite magma evolutions.
66 Indeed, boninite as dykes, veins and pillow lavas is widespread in the Troodos
67 ophiolite complex (e.g. [Cameron, 1979](#); [König et al., 2008](#); [Pearce and Robinson,](#)
68 [2010](#); [Osozawa et al., 2012](#); [Golowin et al., 2017](#); [Woelki et al., 2018](#)). To test this

69 hypothesis, we carried out detailed petrography, mineralogy, major and trace element
70 geochemistry on both interlayered ultramafic suites and representative boninite
71 samples from the Troodos ophiolite. These data, together with petrological modeling
72 and phase equilibrium analysis, support the hypothesis that the interlayered dunite and
73 harzburgite/lherzolite are straightforward consequences of boninite magma evolution
74 in an open magma chamber system with periodic pulses of parental magma supply.
75 The petrological significance is the new understanding on harzburgite petrogenesis.
76 Our study complements previous studies and recognizes the interlayered ultramafic
77 cumulates in the deep crustal section of the Troodos ophiolite complex as a
78 consequence of boninite magma evolution. An important geodynamic implication is
79 that care must be taken when interpreting seismic structure of the ocean crust in
80 subduction settings, especially in rock sequences associated with subduction initiation
81 where much of the boninite magmatism is thought to take place, which is of global
82 significance.

83 In the following, we show our field and petrographic observations, discuss the
84 data, and elaborate reasons that lead to our understanding and conclusions.

85 **2 Geological Setting**

86 The Troodos ophiolite complex is one of the world's best preserved and studied
87 ophiolites, which exposes in the central part of the island of Cyprus in the eastern
88 Mediterranean. A complete ophiolite sequence comprising mantle peridotite,
89 ultramafic to felsic plutonic complex, sheeted dykes, pillow lavas and pelagic
90 sediments has been documented ([Moores and Vine, 1971](#); [Greenbaum, 1972](#)). The

91 Troodos ophiolite can be divided into the northern massif and the southern massif
92 bounded by the Arakapas transform fault zone (Fig. 1). The age of the Troodos
93 ophiolite is 90 – 92 Ma based on U-Pb dating of zircons from plagiogranite in the
94 plutonic section ([Mukasa and Ludden, 1987](#); [Konstantinou et al., 2007](#)), which has
95 been confirmed recently using the advanced zircon U-Pb in situ dating method ([Chen](#)
96 [et al., 2020](#)).

97 Although the Troodos ophiolite complex is well-studied, the tectonic setting in
98 which it was formed remains in dispute. Previous studies suggest that the ophiolite
99 could have formed in a juvenile arc, back-arc, fore-arc, slab-edge or
100 ridge-trench-trench/transform triple junction setting ([Pearce and Robinson, 2010](#);
101 [Osozawa et al., 2012](#); [Regelous et al., 2014](#); [Woelki et al., 2018](#)). Fresh lavas have
102 provided most useful information on the formation of the Troodos ophiolite. There
103 have been varying divisions for the Troodos lavas based on their stratigraphy and
104 geochemistry (e.g., [Smewing et al., 1975](#); [Robinson et al., 1983](#); [Bednarz and](#)
105 [Schmincke., 1994](#); [Pearce and Robinson, 2010](#); [Osozawa et al., 2012](#)). The commonly
106 accepted division includes three major suites: (1) a lower suite (lower pillow lava) of
107 tholeiitic basalt, andesite, dacite to rhyolite, (2) a picritic, basaltic to andesitic upper
108 pillow lava and (3) a boninitic suite cropping out mainly along the Arakapas Fault
109 Zone (e.g., [Flower and Levine, 1987](#); [Thy and Xenophontos, 1991](#)). We use this
110 classification in our discussion for consistency. The boninite lava in Troodos is dated
111 to be ~ 55 Ma based on the Ar-Ar age obtained by [Osozawa et al. \(2012\)](#), about 35
112 Myrs younger than the bulk Troodos ophiolite sequences of ~ 90 Ma (see above),

113 indicating that they are unrelated.

114 The plutonic complex contains a series of ultramafic to gabbroic cumulate rocks
115 overlying the mantle peridotite. The ultramafic cumulates exist in the lower levels of
116 the plutonic complex, overlain by gabbros with or without cross-cutting basaltic dykes.
117 Dunite, wehrlite, websterite and pyroxenite are most documented within the
118 ultramafic cumulates (e.g., [Greenbaum, 1972](#); [Thy, 1987a](#); [Benn and Laurent, 1987](#);
119 [Laurent, 1992](#); [Batanova et al., 1996](#)). The drill hole CY-4 (Fig. 1) sampled gabbros
120 and ultramafic cumulates of coarse-grained websterites containing augite, enstatite,
121 olivine and interstitial plagioclase ([Thy, 1987a](#)). Lowermost dunitic and wehrlitic
122 cumulates were not sampled by the CY-4 drilling. The CY-4 data show that the
123 contact between the lower cumulate complex and the upper gabbros is a petrographic
124 and chemical discontinuity ([Thy et al., 1987a, 1987b](#)), probably in fault contact. In
125 this study, we do not discuss the above cumulate, but focus on the uniquely
126 interlayered dunite-harzburgite/lherzolite cumulate (Fig. 2a-c).

127 **3 Samples and petrography**

128 **3.1 Field observations and samples**

129 The Troodos ophiolite has an inverted stratigraphic sequence with mantle
130 harzburgite on the top of the mountain (Mount Olympus), whereas the lower
131 ultramafic cumulate, gabbros, sheeted dykes and lavas occur downhill in this order
132 (Fig. 1). Therefore, cumulates and lavas are well separated. To test the aforementioned
133 hypothesis on the possible genetic relationship between the interlayered ultramafic

134 cumulate (dunite+harzburgite/lherzolite) and boninite, and to understand the
135 petrogenesis of the ultramafic cumulate, we collected representative samples of the
136 cumulate and boninite for a detailed petrological and geochemical study.

137 Field observations were documented in both northern massif and southern massif
138 of the Troodos ophiolite complex. Our interpreted (hypothesized) ultramafic cumulate
139 comprises serpentinized harzburgite/lherzolite (brown) interlayered with serpentinized
140 dunite (dark grey) (Fig. 2a-c) outcropped on a NW-SE trending ridge, ~ 1 km east of
141 Pano Amiandos, occurring as blocks in fault contact in the vicinity of the “petrologic
142 Moho” between the massive mantle harzburgite (~ 300 m east of mantle harzburgite)
143 and plutonic rocks on the east flank of Mount Olympus (A in Fig.1, Table 1). These
144 blocks are several meters wide and several meters to tens of meters high. The
145 lithological layers vary in thickness from decimeters (Fig. 2a) to millimeters (Fig. 2b)
146 with sharp and parallel contacts. The distinctive cracks perpendicular to the layering
147 are confined in the harzburgite/lherzolite layers (absent in the adjacent dunite layers)
148 (Fig. 2a-c), which is best understood as greater volume expansion of dunite (Ol) than
149 harzburgite/lherzolite (Ol+Opx±Clinopyroxene) during serpentinization (see [Niu et al.,](#)
150 [1997](#)). We sampled the brown and the dark-grey layers of varying thickness.

151 **3.2 Petrography**

152 Boninite samples near the Arakapas Fault Zone (AFZ) contain euhedral to
153 subhedral phenocrysts of olivine, orthopyroxene and spinel (Fig. 3a). Olivine and
154 pyroxene also occur as microlites in the glassy groundmass as the result of fast
155 cooling and quench. The mineralogy and textures of these samples are very similar to

156 the typical boninite from Hahajima Seamount, Bonin forearc (Li et al., 2013) and the
157 modern boninite lava from the Lau Basin (Resing et al., 2011), and confirm the
158 previous studies on the Troodos boninite (e.g., Robinson et al, 1983; Cameron, 1985;
159 Flower and Levin, 1987; Golowin et al., 2017). The absence of plagioclase is a
160 notable feature of typical boninite (e.g., Robinson et al, 1983; Crawford, 1989; Taylor
161 et al., 1994; Resing et al., 2011).

162 Mineral modes of the ultramafic cumulate samples are done by point-counting
163 (Table 1), indicating that the brown layers interlayered with dunite are dominated by
164 harzburgite (locally lherzolite). The dunite layers are strongly serpentinized with only
165 olivine cores left as relics. The dunite is characterized by typical mesh textures with
166 olivine replaced by serpentine (Fig. 3b). In some dunite layers, the olivines are totally
167 serpentinized (see the bottom two dunite layers in Fig. 4). The harzburgite layers are
168 dominated by olivine and orthopyroxene without or with varying amount of
169 clinopyroxene (Cpx), and have undergone varying degree of serpentinization. All the
170 Ol, Opx and Cpx grains are cumulus phases. In most cases, Opx and Ol (~ 0.5 – 1 mm
171 in size) are generally euhedral, showing textually equilibrated mosaic of equigranular
172 grains as adcumulate (Fig. 3c, d). Some olivine grains also exhibit subhedral to
173 anhedral shapes with irregular boundaries (see Fig. 3e, f). The Cpx often occurs as
174 anhedral isolated grains (Fig. 3e, f). Interstitial Cpx also occurs poikilitically
175 enclosing Opx locally. Some orthopyroxene grains have exsolution textures with
176 clinopyroxene lamellae along cleavages (Fig. 3d, f). It is possible that these minute
177 clinopyroxene grains may have developed into the “granular exsolutions” (see Niu,

178 [2004](#)), but most of the coarser-grained ones are clearly liquidus phase. Spinels are
179 generally less than 0.2 mm in size and euhedral to anhedral in shape, often occurring
180 along grain boundaries of Opx and Ol.

181 In order to show microscopic textures of the interlayered dunite and
182 harzburgite/lherzolite cumulate as a whole, we piece together low magnification
183 photomicrographs of a cumulate sample (TDS45-4) with relatively thin layers (2 – 15
184 mm) collected from the block shown in Fig. 2b (Fig. 4). The layers are well defined
185 with clear contacts and transitions. The mineral modes given in Fig. 4 indicate that the
186 harzburgite layers have varying Cpx and may be locally termed lherzolite if Cpx \geq 10
187 vol. % (not in this mosaic). The harzburgite shows typical cumulate texture though
188 camouflaged by varying degrees of serpentinization with layer-perpendicular cracks
189 filled with serpentines (see above and below). The dunite is strongly serpentinized,
190 with few olivine relics in some of the layers. Spinels often appear as euhedral or
191 subhedral crystals in the harzburgite layers, while fine-grained magnetite aggregates
192 occur as bands in the interiors of the serpentine veins in dunite layers (Fig. 4 left). The
193 layer-perpendicular cracks are filled with serpentines coming from the dunite layers.
194 All the primary phases are subjected to serpentinization, but the rate and extent of
195 serpentinization decrease in the order Ol, Opx and Cpx, with Ol-dominated dunite
196 having volume expansion of up to ~ 30 wt. %, significantly more than harzburgite
197 (locally lherzolite) made up of Ol+Opx±Cpx ([Coleman, 1971](#); [O'Hanley, 1992](#); [Niu et](#)
198 [al., 1997](#)). As a result, the greater volume expansion of dunite layers causes
199 layer-perpendicular cracks (filled with serpentines) in the adjacent

200 harzburgite/lherzolite layers on both macroscopic (Fig. 2) and microscopic (Fig. 4)
201 scales.

202 **4 Methods**

203 **4.1 Sample preparation**

204 To study the petrographic details of the interlayered cumulate of dunite and
205 harzburgite/lherzolite, we sampled the cumulate on millimeter scales (see Fig. 2b) for
206 texture characterization and mineral analysis (TDS06 and TDS45). Two samples with
207 layers of 2 – 5 cm thick (see Fig. 2c) were also collected for “bulk-rock” analysis
208 (TDS46 and TDS47). The harzburgite interlayered with dunite in TDS46 is locally of
209 high Cpx (vs. seen in Fig. 4) and is best termed lherzolite on the petrographic scale
210 (see Table 1). In order to show the different chemical compositions between the
211 brown and dark-grey layers, the two cumulate samples were cut carefully into 5
212 pieces of “pure” dunite and 4 pieces of “pure” harzburgite/lherzolite with surface
213 contaminants thoroughly removed. Although the “bulk-rock” samples are variably
214 serpentinized, the compositions of the cumulate dunite and harzburgite/lherzolite can
215 be compared on an anhydrous basis (see [Niu, 2004](#)) by normalizing major element
216 compositions to 100%. These 9 sample fragments were then reduced to small (1 – 2
217 cm) chips and ultrasonically washed in Milli-Q water before dried and grinded into
218 powder using agate mill in a clean environment for “bulk-rock” analysis.

219 Boninite samples from pillow lavas and dykes near the AFZ have phenocrysts
220 and quenched microlites. To obtain melt compositions, 9 boninite samples were

221 crushed into chips of 1 – 2 mm size, and only groundmass fractions free of
222 phenocrysts were hand-picked under a binocular before ultrasonically cleaned in
223 Milli-Q water. These chips were then embedded in epoxy and polished for
224 laser-ablation inductively coupled plasma-mass spectrometer (LA-ICP-MS) analysis.

225 **4.2 Analytical methods**

226 Bulk-rock major element analysis of the interlayered ultramafic cumulate was
227 done in the Laboratory of Ocean Lithosphere and Mantle Dynamics, Institute of
228 Oceanology, Chinese Academy of Sciences (LOLMD-IOCAS) by using Agilent 5100
229 inductively coupled plasma-optical emission spectrometer (ICP-OES) following the
230 method of [Kong et al. \(2019\)](#). The analytical precision is better than 5% (RSD,
231 relative standard deviation). The values of USGS reference materials BCR-2,
232 BHVO-2 and AGV-2 analyzed together with the samples agree well with the
233 reference values within error.

234 For trace element analysis, 50 mg powder of each cumulate sample was dissolved
235 with acid mix (1 : 2) of distilled HF and aqua regia (1 HNO₃: 3 HCl) in a 15 mL
236 Teflon beaker. The analysis was done using an Agilent 7900 inductively coupled
237 plasma-mass spectrometer (ICP-MS) in the LOLMD-IOCAS following [Chen et al.](#)
238 [\(2017\)](#). USGS reference rocks (BCR-2, BHVO-2, AGV-2, GSP-2 and W-2) analyzed
239 as unknowns along with the samples give compositions the same as recommended
240 values within error.

241 Major and trace elements of boninite samples and minerals (olivine,
242 orthopyroxene, clinopyroxene and spinel) in the interlayered ultramafic cumulate

243 samples were analyzed using a Photon Machines Excite 193 nm excimer Ar-F laser
244 system attached to an Agilent 7900 ICP-MS in the LOLMD-IOCAS. Spot size used
245 for analyzing glasses and lavas was 110 μm . For minerals, spot sizes were 85 μm for
246 olivine, orthopyroxene and clinopyroxene and 25 μm for spinel. An energy density of
247 3.94 J/cm^2 at a repetition rate of 6 Hz were applied. Each analysis includes 25 s
248 background acquisition (gas blank) followed by 50 s data acquisition. USGS glasses
249 (BCR-2G, BHVO-2G and BIR-1G) were used as multiple reference materials for
250 external calibration following [Liu et al. \(2008\)](#). In combination with the summed
251 metal oxide normalization method and time-drift correction according to the
252 variations of NIST 610, the matrix effect and instrumental drift can be effectively
253 corrected ([Liu et al., 2008](#)). The raw data were processed using
254 ICPMSDataCal_ver11.0 ([Liu et al., 2008](#)). Data quality was assessed by the result of
255 USGS reference materials and the repeated analyses of GSE-1G over the analytical
256 session (Supplementary Table S1, S2). For major elements with concentrations > 0.1
257 wt. %, the accuracies (relative error between measured and recommended values) and
258 precisions (RSD) for USGS glasses are generally better than 5 %. The reproducibility
259 of GSE-1G is better than 5% for most of the major element analyses of glass, olivine,
260 pyroxene and spinel, except for TiO_2 , Cr_2O_3 , MnO , NiO , ZnO and V_2O_5 (RSD < 10%)
261 in spinel analysis, which is due to the small ablation spot size (25 μm). For most trace
262 elements, the accuracy and precision of USGS glasses and GSE-1G are better than 5%
263 (Supplementary Table S3). The analytical details are given in [Xiao et al. \(2020\)](#).

264 **5 Results**

265 **5.1 Major and trace element compositions of the boninite**

266 There are recent analyses on fresh boninite glasses from the Troodos ophiolite
267 available (König et al., 2008; Golowin et al., 2017; Woelki et al., 2018). Here we
268 present some new data on major and trace elements of boninite pillow lavas and dykes
269 from the AFZ (Table 2).

270 The major element compositions of the samples near the AFZ are consistent with
271 typical boninite ($\text{MgO} > 8$ wt. %, $\text{TiO}_2 < 0.5$ wt. % and $\text{SiO}_2 > 52$ wt. %; Le Bas,
272 2000). The slightly more evolved samples with lower MgO (7.0 – 7.3 wt. %) are
273 similar to the compositions of some boninite glass samples (Golowin et al., 2017;
274 Woelki et al., 2018). The Troodos boninite is classed as high-Ca boninite because of
275 the high $\text{CaO}/\text{Al}_2\text{O}_3$ value (always > 0.75 ; Crawford, 1989), while boninite samples in
276 this study have $\text{CaO}/\text{Al}_2\text{O}_3$ of 0.48 – 0.75. The trace element compositions of the
277 boninite near the AFZ overlap well with the literature data on boninite glasses
278 (Golowin et al., 2017; Woelki et al., 2018; Fig. 5). The REE patterns of the boninite
279 samples show obvious “U shape” (Fig. 5a), and there is notable enrichment in fluid
280 soluble elements (e.g., Ba, Rb, U, Sr and Pb) in boninite samples characteristic of
281 subduction-related magmas (Fig. 5b). The U-shaped REE pattern is characteristic of
282 boninite magmas as a result of addition of light rare earth element (LREE) enriched
283 component to a refractory peridotite mantle source (Cameron, 1983; Crawford, 1989).
284 All these observations confirm that the boninite samples near the AFZ are typical
285 boninite.

286 **5.2 Bulk-rock major and trace elements of the interlayered ultramafic cumulate**

287 Bulk-rock major and trace element compositions of 5 dunite and 4 lherzolite
288 (locally Cpx rich from the harzburgite layer; see above) cumulate samples are given in
289 Table 3. The major element compositions are normalized to 100 % on an anhydrous
290 basis because of serpentinization related loss on ignition (LOI: 6.0 – 12.8 wt. % for
291 dunite and < 1.6 wt. % for lherzolite from locally Cpx rich harzburgite layer). The
292 data show obvious differences between the dark grey (dunite) and brown
293 (harzburgite/lherzolite) layers as expected on the basis of field and petrographic
294 observations. The dark grey layers have lower average SiO₂ (44.42 wt. %), Al₂O₃
295 (0.43 wt. %), CaO (0.27 wt. %), but higher FeOt (11.84 wt. %) and MgO (44.61
296 wt. %), whereas the brown layers have higher average SiO₂ (52.52 wt. %), Al₂O₃ (1.7
297 wt. %), CaO (5.75 wt. %), but lower FeOt (7.99 wt. %) and MgO (31.76 wt. %). In
298 terms of bulk-rock incompatible trace element compositions, the lherzolite from
299 locally Cpx rich harzburgite layer has similar characteristics (U-shaped REE pattern
300 and enrichment in fluid soluble elements, see above) but lower concentration levels
301 than the Troodos boninite (Fig. 5), which indicates a possible genetic link between the
302 two.

303 **5.3 Mineral chemistry**

304 The average major element compositions of olivine, spinel, orthopyroxene and
305 clinopyroxene and trace element compositions of orthopyroxene and clinopyroxene in
306 different samples are given in Table 4 and Table 5 with individual analyses given in
307 Supplementary Table S4 – S7.

308 The forsterite content for olivine (Fo) from the cumulate dunite varies from 87 to
309 89. The olivine phenocrysts in boninite glasses from the literature ([Golowin et al.,](#)
310 [2017](#)) are more Mg-rich (the mean Fo is 89) with a larger Fo range (85 – 91) (Fig. 6).
311 This indicates that the melt in equilibrium with olivine from the cumulate dunite is
312 more evolved than the erupted boninite melt. This is expected in an evolving magma
313 chamber with multiple pulses of melt injection (see below). We didn't have the
314 composition of olivine in the harzburgite/lherzolite layer because of pervasive of
315 serpentinization with very rare relicts for analysis.

316 Orthopyroxene and clinopyroxene are both observed in the cumulate
317 harzburgite/lherzolite. We analyzed 55 Opx grains and 33 Cpx grains from the
318 harzburgite/lherzolite layers (Table 5). The Mg# varies from 0.88 to 0.89 and 0.89 to
319 0.91 in Opx and Cpx respectively. Orthopyroxene has lower CaO (0.97 – 3.99 wt. %),
320 TiO₂ (0.02 – 0.03 wt. %), Cr₂O₃ (0.42 – 0.63 wt. %), slightly lower Al₂O₃ (1.25 – 1.64
321 wt. %) and higher MgO (31.73 – 33.52 wt. %), FeOt (7.00 – 7.84 wt. %), SiO₂ (53.71
322 – 56.49 wt. %) than clinopyroxene. The major element compositions of Cpx in the
323 cumulate harzburgite/lherzolite differ greatly from those in mantle harzburgite of the
324 Troodos ophiolite ([Batanova and Sobolev, 2000](#)) with lower Mg#, CaO, Al₂O₃, Cr₂O₃
325 and higher FeOt (Fig. 7). The ultramafic cumulates collected by [Coogan et al. \(2003\)](#)
326 show large Cpx major element compositional variations, but the Cpx in the ultramafic
327 cumulates near the Amiandos we study shows quite uniform composition (Fig. 7). For
328 trace element compositions, Opx has N-MORB normalized incompatible element
329 patterns similar to those of Cpx and boninite, but has lower concentrations (see

330 below).

331 Twenty spinel crystals from the cumulate harzburgite and dunite were analyzed
332 with varying Cr₂O₃ (39.24 – 45.56 wt. %), Al₂O₃ (15.56 – 21.01 wt. %) and TiO₂
333 (0.11 – 0.18 wt. %). In the trivalent Cr-Al-Fe³⁺ ternary cation diagram (Fig. 8a), the
334 spinels in the ultramafic cumulate fall within the ophiolite chromite compositional
335 field between the fields of boninite and abyssal peridotite spinels, which can be
336 classified as Al-chromite (Stevens, 1944). Compared with the compositions of spinel
337 in boninite glass of the Troodos ophiolite (Golowin et al., 2017; Woelki et al., 2018),
338 spinels in the ultramafic cumulate have lower Cr# (Cr# = Cr/(Cr+Al) = 0.56 – 0.64
339 with an average of 0.61) and slightly higher Mg# (Mg# = Mg/(Mg+Fe²⁺) = 0.39 –
340 0.57 with an average of 0.48), which is similar to forearc peridotite (Fig. 8b),
341 suggesting a subducting-zone setting.

342 **6 Discussion**

343 **6.1 Petrographic evidence for genetic link of boninite with the layered ultramafic** 344 **cumulate**

345 As shown above, boninite samples near the AFZ contains phenocrysts of olivine,
346 orthopyroxene and spinel with olivine and pyroxene microlites without plagioclase
347 (Fig. 3a), characteristic of typical boninite (e.g., Crawford, 1989; Taylor et al., 1994;
348 Resing et al., 2011; Li et al., 2013). Experimental studies on the petrogenesis of
349 boninite indeed indicate that olivine and orthopyroxene are primary liquidus phases
350 followed by clinopyroxene with plagioclase (Plg) appearing very late on the liquidus

351 (Duncan and Green, 1987; Falloon and Danyushevsky, 2000). Studies on boninite
352 from the AFZ further show a crystallization order of chromite, olivine, orthopyroxene,
353 clinopyroxene and plagioclase, which differs from basalt, basaltic andesite and
354 andesite glasses from the upper pillow lava that are consistent with a crystallization
355 order of chromite, olivine, clinopyroxene and plagioclase (Flower and Levine, 1987;
356 Thy and Xenophontos, 1991). We can thus reason that the dunite (Ol) and
357 harzburgite/lherzolite (Ol+Opx±Cpx) cumulate must have formed as a straightforward
358 consequence of boninite magma evolution. Indeed, the crystallization order of the
359 ultramafic cumulate from the Pano Amiandos is reported as Ol → Opx → Cpx → Plg
360 (Chum, 2014), which is different from that of the ultramafic cumulate commonly
361 found in the Troodos ophiolite such as in the drill hole CY-4 (Ol → Cpx → Opx →
362 Plg; George, 1978; Thy, 1987b; Browning et al., 1989). These observations and
363 understanding thus point to the genetic link between the boninite (Fig. 2d-f) and the
364 interlayered cumulate of dunite and harzburgite/lherzolite (Fig. 2a-c).

365 **6.2 Major element compositional evidence for genetic link of boninite with the** 366 **layered ultramafic cumulate**

367 Spinel has been shown to be an effective tool to constrain parental melt
368 compositions of cumulate rocks (e.g. Arai, 1994; Kamenetsky et al., 2001; Rollinson,
369 2008; Allahyari et al., 2014; Saccani and Ferrara, 2015). Experimental studies have
370 shown direct relationship between compositions of melt and spinel in terms of Al₂O₃
371 and TiO₂ (Kamenetsky et al., 2001; Wasylenki et al., 2003). Rollinson (2008) has
372 derived expressions using spinel compositions to calculate Al₂O₃ and TiO₂ contents in

373 parental melts in arc-type settings:

$$374 \quad \text{Al}_2\text{O}_3 (\text{melt}) = 5.2181 \times \text{Ln} (\text{Al}_2\text{O}_3 \text{ in spinel}) - 1.0505$$

$$375 \quad \text{TiO}_2 (\text{melt}) = 1.0963 \times \text{TiO}_2 (\text{spinel})^{0.7863}$$

376 Using this approach, we calculated Al_2O_3 and TiO_2 contents of the parental melt
377 in equilibrium with spinels in the cumulate dunite and harzburgite/lherzolite (Fig. 9).
378 Contents of Al_2O_3 and TiO_2 in boninite glasses from the literature (Woelki et al., 2018)
379 and different tectonic settings are shown for comparison. The inferred melt has
380 relatively lower Al_2O_3 (13.27 – 14.84 wt. %) and TiO_2 (0.19 – 0.28 wt. %) than
381 MORB and island arc tholeiite (IAT). The Al_2O_3 and TiO_2 contents in boninite glasses
382 (13.38 – 15.24 wt. % and 0.25 – 0.38 wt. %, respectively) are similar to those of the
383 calculated melt parental to the cumulate dunite and harzburgite/lherzolite, in support
384 of the hypothesis that the interlayered dunite and harzburgite/lherzolite cumulate of
385 Troodos is most likely the product crystallized from a boninite parental magma.

386 **6.3 Trace element compositional evidence for genetic link of boninite with the** 387 **layered ultramafic cumulate**

388 If the cumulate harzburgite/lherzolite (and dunite) is indeed the crystallization
389 product of the evolving boninite melt, the minerals in harzburgite/lherzolite should be
390 in equilibrium with the melt represented by boninite lavas in the Troodos ophiolite.
391 By using mineral-melt partition coefficients, we calculated the incompatible trace
392 element compositions of melts in equilibrium with average compositions of
393 clinopyroxene ($\text{Mg}\# = 0.90$) and orthopyroxene ($\text{Mg}\# = 0.89$) in the cumulate
394 harzburgite/lherzolite.

395 Abundant pyroxene/melt partition coefficients (Kd's) are available in the
396 literature for anhydrous basaltic systems (see [Niu et al., 1996](#); [Bédard, 1999, 2001](#);
397 [Klemme et al., 2002](#)), but rare for hydrous basalt and boninite melts. Because the
398 relevant incompatible element Kd's for wet hydrous systems are 2-3 times lower than
399 in anhydrous melts (see [McDade et al., 2003](#)), we use the Kd data for dry basalts with
400 half of the values in our calculation (Supplementary Table S8). Fig. 10 shows
401 N-MORB normalized incompatible element patterns of such calculated melts in
402 equilibrium with clinopyroxene and orthopyroxene in the cumulate
403 harzburgite/lherzolite. The incompatible element patterns of calculated melts in
404 equilibrium with both Cpx and Opx show remarkable similarity to those of the
405 Troodos boninite lavas (Fig. 10). There is also significant correlation for all the
406 incompatible element abundances between the calculated melts in equilibrium with
407 Cpx and Opx ($R_{\text{Cpx-melt}} = 0.95$ and $R_{\text{Opx-melt}} = 0.93$) and the average Troodos boninite
408 glass composition. Most incompatible elements of the calculated melts overlap well
409 with those of boninite samples (boninite glasses from the literature and boninite
410 samples in this study) (Fig. 10).

411 The remarkable similarity in incompatible element abundances and systematics
412 we present here offer evidence that the orthopyroxene and clinopyroxene in the
413 cumulate harzburgite/lherzolite are in equilibrium with melts represented by the
414 boninite in the Troodos ophiolite. Some of the mantle harzburgites/dunites in Troodos
415 have been shown to be equilibrated with the migrating melts (boninites or some
416 depleted unknown melts) and are suggested to be formed by melt percolation or

417 melt-rock reaction (Batanova and Sobolev, 2000; Büchl et al., 2002). However, the
418 ultramafic rocks we study are not deformed massive mantle residual harzburgite with
419 irregular dunite dikes and veins, but have typical cumulate textures (Figs. 3 & 4) and
420 harzburgite/lherzolite-dunite interlayering (Fig. 2a-c). Moreover, in terms of mineral
421 chemistry, the interlayered harzburgite/lherzolite-dunite rocks have lower Fo of
422 olivine (87-89), lower Mg# and higher FeO_T of Cpx (see Fig. 8) than the mantle
423 dunite and harzburgite that have undergone melt percolation (Batanova and Sobolev,
424 2000; Büchl et al., 2002). Hence, the data and understanding support our hypothesis
425 that the interlayered harzburgite/lherzolite-dunite rocks in Troodos are of cumulate
426 origin resulting from boninite magma evolution.

427 **6.4 Liquid lines of descent evidence for genetic link of boninite with the layered** 428 **ultramafic cumulate**

429 We use Petrolog 3.1.1.3 software (Danyushevsky and Plechov, 2011) to simulate
430 the liquid lines of descent (LLDs) of the Troodos boninite. The primary magma
431 compositions for the Troodos boninite lavas can be inferred by calculation or using
432 olivine melt inclusions (Duncan and Green, 1980; Portnyagin, 1997; Falloon and
433 Danyushevsky, 2000; Golowin et al., 2017). We choose a primary Troodos boninite
434 magma composition used by Golowin et al. (2017) because it was calculated from a
435 boninite glass sample near the AFZ (TRV-353, Supplementary Table S9). High water
436 content in the primary boninite magma is estimated in the literature (e.g. Thy, 1987a;
437 Dobson et al., 1995; Sobolev and Chaussidon, 1996; Falloon and Danyushevsky,
438 2000). We use a water content of 4 wt. % in the modeling. The initial oxidation state

439 of magma is set to be QMF+1 (Pearce and Robinson, 2010). Olivine, plagioclase,
440 clinopyroxene and orthopyroxene are chosen as possible liquidus phases.

441 The modeled compositions of the residual melts (Fig. 11) and the crystallized
442 cumulate (dunite, harzburgite and lherzolite, Supplementary Table S10) are most
443 consistent with the compositions of boninite glasses and the interlayered ultramafic
444 cumulate under 0.1 GPa. The liquidus minerals appear in the order of olivine (at
445 $\text{MgO}_{\text{melt}} = 14.8$ wt. %), orthopyroxene (at $\text{MgO}_{\text{melt}} = 10.9$ wt. %), clinopyroxene (at
446 $\text{MgO}_{\text{melt}} = 8.9$ wt. %) and plagioclase (very late, at $\text{MgO}_{\text{melt}} = 3.3$ wt. %) (Fig. 11). In
447 the modeling, dunite, harzburgite and lherzolite can be produced after 1 ~ 14 %, 15 ~
448 24 % and 25 ~ 29 % crystallization respectively (see Supplementary Table S10). The
449 LLD paths of major elements of the melt overlap well with the data from the boninite
450 glasses (Fig. 11). Meanwhile, the Mg# of the modeled melt after 12 ~ 23 %
451 crystallization (Mg# = 0.66 ~ 0.73) is very close to that of the boninite glass (Mg# =
452 0.65 ~ 0.72; Woelki et al., 2018), which shows similar degree of magma evolution.
453 The modeling also indicates that fractional crystallization of boninite may occur at a
454 shallow depth (~ 3 km) in a magma chamber. In summary, the modeling results match
455 well with the compositions of both the ultramafic cumulate (i.e., rocks with the
456 assemblage of the liquidus minerals: Ol → Ol+Opx → Ol+Opx+Cpx) and the
457 boninite melt, which offer another line of evidence further in support of our
458 hypothesis that the interlayered dunite (Ol) and harzburgite/lherzolite (Ol+Opx±Cpx)
459 cumulate in the Troodos ophiolite is the product of fractional crystallization of
460 boninite magmas.

461 **6.5 Development of the interlayered dunite and harzburgite/lherzolite during**
462 **boninite magmatism**

463 The foregoing demonstrations using petrography, mineral chemistry, and melt
464 modeling offer strong lines of evidence in support of our hypothesis that the
465 interlayered dunite-harzburgite/lherzolite rocks in the Troodos ophiolite complex (Fig.
466 2a-c) are of cumulate origin resulting from boninite magma evolution. We now show
467 how the interlayered dunite and harzburgite (locally lherzolite) cumulate may have
468 developed in terms of understood phase equilibria during boninite magma evolution.

469 As boninite has liquidus phases of Ol, Opx and minor Cpx, we can examine the
470 phase relationships involving melt-Ol-Opx-Cpx to illustrate the development of the
471 interlayered dunite and harzburgite/lherzolite cumulate. Experimental studies on
472 multiple component natural systems are rare, but available experimental data on
473 simple SiO₂-MgO-CaO system with melt-Fo-En-Di endmember phase equilibria can
474 be used to approximate the natural melt-Ol-Opx-Cpx system to illustrate the concept
475 and development of the inter-layered dunite-harzburgite cumulate. Because of the
476 incongruent melting of enstatite at the pressure < 2 GPa ([Presnall et al., 1978](#)), very
477 few experimental studies focusing directly on the Fo-En-Di system. However, we can
478 construct a ternary Fo-En-Di phase diagram using existing experimental data ([Davis](#)
479 [and England, 1964](#); [Boyd et al., 1964](#); [Williams and Kennedy, 1969](#); [Kushiro, 1969](#);
480 [Presnall et al., 1978](#); [Inoue, 1994](#)) to illustrate the concept as shown in Fig. 12. The
481 temperature contours are for the Fo-En-Di system at 2 GPa would be significantly
482 lower for multi-component natural systems especially for the hydrous boninitic

483 systems, and the position of the eutectics may shift slightly under hydrous condition
484 and lower pressure (Kushiro, 1969; van der Laan, 1987), but the concept we illustrate
485 is valid and insightful as melt evolves and crystallization takes place during cooling.

486 Assuming point A (Fig. 12) represents the composition of the primary boninite
487 magma, it begins to crystallize forsterite with cooling, leading to the melt move away
488 from Fo towards the Fo-En cotectic while precipitating dunite cumulate in a magma
489 chamber (A→B in Fig. 12). Continued cooling and crystallization of Fo with dunite
490 cumulate formation, the melt eventually reaches the Fo-En cotectic and both Fo and
491 En coprecipitate to form harzburgite cumulate overlaying the earlier dunite layer
492 (C→D in Fig. 12). Periodic primary boninite melt replenishment into the magma
493 chamber will result in the above process to repeat, thus leading to the interlayered
494 dunite-harzburgite cumulate (Fig. 2a-c). The thickness of individual layers depends on
495 both the frequency of melt supply pulses and the volume of each melt pulse.
496 Importantly, delayed melt supply can lead to Fo-En coprecipitation along the cotectic
497 line to reach the Fo-En-Di eutectic (E in Fig. 12), leading to the coprecipitation of
498 clinopyroxene and the formation of harzburgite with minor Cpx or localized lherzolite,
499 which is consistent with our observations (see above).

500 The formation of interlayered dunite-harzburgite/lherzolite cumulate in the Troodos
501 ophiolite complex can be briefly summarized as crystallization of boninite magma
502 and periodic magma injections into an open magma chamber as illustrated in Fig. 12,
503 in cycles of a → b → c → (d) → a → b → c → (d)...

504 Magmatic layering could be caused by several processes such as convection-related

505 processes ([Naslund et al., 1991](#)) and deformation of crystal mush ([Jousselin et al.,](#)
506 [2012](#)). These could be other processes taking place in the magma chamber, but all
507 these speculations are hard to test. Besides, mechanical processes such as
508 gravitational sorting are unlikely because our observed layers are generally quite thin
509 and as thin as millimeters without grain size grading. Our hypothesis is the simplest
510 and is physically most plausible process that agrees with the petrologic and
511 geochemical characteristics.

512 Corresponding to the phase equilibrium analysis (Fig. 12), Figure 13 illustrates
513 the evolution of boninite magma and the petrogenesis of the interlayered
514 dunite-harzburgite/lherzolite cumulate. Boninite melt originates from high degree
515 partial melting of refractory harzburgitic mantle sources as the result of water
516 introduction at high temperatures ([Kostopoulos and Murton, 1992](#); [Falloon and](#)
517 [Danyushevsky, 2000](#); [Li et al., 2013](#)). Crystallization of boninite melt in an open
518 magma chamber leads to the formation of the interlayered
519 dunite-harzburgite/lherzolite cumulate (Fig. 13a). The parental melt begins to
520 crystallize olivine to form a dunite layer (A→C in Fig. 12), and the continued
521 crystallization along the Fo-En cotectic and Fo-En-Di eutectic will produce
522 harzburgite/lherzolite layer (C→D→E in Fig. 12) (Fig. 13b). Primitive melt with high
523 temperature and high Mg# (Mg#₁) injects into the magma chamber, which, mixed
524 with some existing melt, will soon erupt under increased pressure (Mg#₂). The
525 unerupted melt can mix more thoroughly with the evolved melts in the magma
526 chamber to continue the crystallization as above (Mg#₃), forming layered

527 dunite-harzburgite/lherzolite cumulate (Fig. 13c-e, f). It is important to note that this
528 repeated cycling process will lead to melt compositional changes with $Mg\#_1 > Mg\#_2 >$
529 $Mg\#_3$ (Fig. 13c). Hence, olivine phenocrysts from boninite glasses have higher Fo
530 than olivine in the cumulate (Fig. 6).

531 **7 Conclusions**

532 In this paper, we report the interlayered dunite-harzburgite/lherzolite rock
533 association in the Troodos ophiolite complex. We hypothesize that this rock
534 association is of magmatic cumulate origin as the result of boninite magma evolution.
535 We have successfully tested and proved this hypothesis by using field and
536 petrographic observations, mineral chemistry, major and trace element compositions,
537 petrological modeling, and phase equilibrium analysis.

538 (1) This understanding represents an important novel petrological contribution.

539 (2) With Ol and Opx being the liquidus phases and with the interlayered dunite
540 (Ol)-harzburgite/lherzolite (Ol+Opx±Cpx) rock association, we hypothesize that
541 the latter is of cumulate origin as a result of straightforward consequence of
542 boninite magma evolution.

543 (3) The melts in equilibrium with spinels in the cumulate harzburgite/lherzolite and
544 dunite are characteristically boninitic in terms of major element compositions (e.g.,
545 TiO_2 and Al_2O_3).

546 (4) The calculated melts in equilibrium with Cpx and Opx in the cumulate
547 harzburgite/lherzolite share the same trace element patterns as the Troodos
548 boninite (both glasses and bulk-rock compositions).

- 549 (5) Petrological modeling of the boninite melt evolution shows a crystallization order
550 of $Ol \rightarrow Opx \rightarrow Cpx \rightarrow Plg$, indicating that the cumulate dunite and harzburgite
551 (locally lherzolite) in the Troodos ophiolite can be produced by fractional
552 crystallization of the primary boninite melt at 0.1 GPa.
- 553 (6) The petrogenesis of the interlayered dunite-harzburgite/lherzolite cumulate is best
554 understood as the result of fractional crystallization of periodically replenished
555 and periodically erupted open magma chamber with the primitive boninite melt
556 derived from depleted mantle sources.
- 557 (7) We emphasize it important to consider dunite-harzburgite/lherzolite cumulate
558 when interpreting seismic structure of the crust in subduction settings, especially
559 in rock sequences associated with subduction initiation thought to be indicated by
560 boninite magmatism.

561 **Acknowledgements**

562 We thank the company of Iain Neill, Peter Tollan and Durham 3rd year students during
563 our annual Troodos field trips. We thank Akihiro Tamura and anonymous reviewers
564 for constructive reviews, and Michael Roden for editorial handling. This study is
565 supported by the National Natural Science Foundation of China (41630968), the
566 NSFC-Shandong Joint Fund for Marine Science Research Centers (U1606401), the
567 National Natural Science Foundation of China (91958215), Qingdao National
568 Laboratory for Marine Science and Technology (2015ASKJ03), and the 111 Project
569 (B18048).

570 **References**

- 571 Allahyari, K., Saccani, E., Rahimzadeh, B., Zeda, O., 2014. Mineral chemistry and
572 petrology of highly magnesian ultramafic cumulates from the Sarve-Abad
573 (Sawlava) ophiolites (Kurdistan, NW Iran): New evidence for boninitic
574 magmatism in intra-oceanic fore-arc setting in the Neo-Tethys between Arabia
575 and Iran. *Journal of Asian Earth Sciences* 79, 312-328.
- 576 Arai, S., 1994. Characterization of spinel peridotites by olivine-spinel compositional
577 relationships: review and interpretation. *Chemical Geology* 113, 191-204.
- 578 Barnes, S.J. and Roeder, P.L., 2001. The range of spinel compositions in terrestrial
579 mafic and ultramafic rocks. *Journal of petrology* 42, 2279-2302.
- 580 Batanova, V.G., Sobolev, A.V., Schmincke, H.U., 1996. Parental melts of the intrusive
581 cumulates of the Troodos massif, Cyprus: a study of clinopyroxenes and melt
582 inclusions in plagioclase. *Petrology* 4, 255-264.
- 583 Batanova, V.G., Sobolev, A.V., 2000. Compositional heterogeneity in
584 subduction-related mantle peridotites, Troodos massif, Cyprus. *Geology* 28,
585 55-58.
- 586 Bédard, J.H., 1999. Petrogenesis of boninites from the Betts Cove ophiolite,
587 Newfoundland, Canada: identification of subducted source components. *Journal*
588 *of Petrology* 40, 1853-1889.
- 589 Bédard, J.H., 2001. Parental magmas of the Nain Plutonic Suite anorthosites and
590 mafic cumulates: a trace element modelling approach. *Contributions to*
591 *Mineralogy and Petrology* 141, 747-771.

592 Bednarz, U., Schmincke, H., 1994. Petrological and chemical evolution of the
593 northeastern Troodos Extrusive Series, Cyprus. *Journal of Petrology* 35,
594 489-523.

595 Benn, K., Laurent, R., 1987. Intrusive suite documented in the Troodos ophiolite
596 plutonic complex, Cyprus. *Geology* 15, 821-824.

597 Boyd, F., England, J., Davis, B.T., 1964. Effects of pressure on the melting and
598 polymorphism of enstatite, $MgSiO_3$. *Journal of Geophysical Research* 69,
599 2101-2109.

600 Browning, P., Roberts, S., Alabaster, T., 1989. Fine scale modal layering and cyclic
601 units in ultramafic cumulates from the CY-4 borehole, Troodos ophiolite:
602 evidence for an open system magma chamber. *Cyprus Crustal Study Project:*
603 *Initial Report, Hole CY-4, Geological Survey of Canada, pp.193-220.*

604 Büchl, A., Brüggemann, G., Batanova, V.G., Münker, C., Hofmann, A.W., 2002. Melt
605 percolation monitored by Os isotopes and HSE abundances: a case study from
606 the mantle section of the Troodos Ophiolite. *Earth and Planetary Science Letters*
607 204, 385-402.

608 Cameron, W.E., Nisbet, E.G., Dietrich, V.J., 1979. Boninites, komatiites and ophiolitic
609 basalts. *Nature* 280, 550.

610 Cameron, W.E., McCulloch, M.T., Walker, D.A., 1983. Boninite petrogenesis:
611 chemical and Nd-Sr isotopic constraints. *Earth and Planetary Science Letters* 65,
612 75-89.

613 Cameron, W.E., 1985. Petrology and origin of primitive lavas from the Troodos

614 ophiolite, Cyprus. *Contributions to Mineralogy and Petrology* 89, 239-255.

615 Cawthorn, R.G. (Ed), 1996. *Layered Intrusions*. Elsevier, New York, pp. 531.

616 Charlier, B., Namur, O., Latypov, R., Tegner, C. (Eds), 2015. *Layered Intrusions*.

617 Springer, London, pp. 748.

618 Chen, S., Wang, X., Niu, Y., Sun, P., Duan, M., Xiao, Y., Guo, P., Gong, H., Wang, G.,

619 Xue, Q., 2017. Simple and cost-effective methods for precise analysis of trace

620 element abundances in geological materials with ICP-MS. *Science Bulletin* 62,

621 277-289.

622 Chen, Y., Niu, Y., Shen, F., Gao, Y., Wang, X., 2020. New U-Pb zircon age and

623 petrogenesis of the plagiogranite, Troodos ophiolite, Cyprus. *Lithos*

624 (<https://doi.org/10.1016/j.lithos.2020.105472>)

625 Chum, C., 2014. Cumulate pyroxenite and pyroxenite dykes in the Troodos ophiolite,

626 Cyprus. Master dissertation, The University of Hongkong.

627 Coleman, R.G., Keith, T.E., 1971. A chemical study of serpentinization—Burro

628 Mountain, California. *Journal of Petrology* 12, 311-328.

629 Coogan, L., Banks, G., Gillis, K., MacLeod, C., Pearce, J., 2003. Hidden melting

630 signatures recorded in the Troodos ophiolite plutonic suite: evidence for

631 widespread generation of depleted melts and intra-crustal melt aggregation.

632 *Contributions to Mineralogy and Petrology* 144, 484-506.

633 Crawford, A.J., Falloon, T.J., Green, D.H., 1989. Classification, petrogenesis and

634 tectonic setting of boninites.

635 Danyushevsky, L.V., Plechov, P., 2011. *Petrolog3: Integrated software for modeling*

636 crystallization processes. *Geochemistry, Geophysics, Geosystems* 12,
637 doi:10.1029/2011GC003516.

638 Davis, B., England, J., 1964. The melting of forsterite up to 50 kilobars. *Journal of*
639 *Geophysical Research* 69, 1113-1116.

640 Dick, H.J.B., Fisher, R.L., Bryan, W.B., 1984. Mineralogical variability of the
641 uppermost mantle along mid-ocean ridges. *Earth and Planetary Science Letters*
642 69, 88-106.

643 Dobson, P.F., Skogby, H., Rossman, G.R., 1995. Water in boninite glass and
644 coexisting orthopyroxene: concentration and partitioning. *Contributions to*
645 *Mineralogy and Petrology* 118, 414-419.

646 Duncan, R.A., Green, D., 1980. Role of multistage melting in the formation of
647 oceanic crust. *Geology* 8, 22-26.

648 Duncan, R.A., Green, D.H., 1987. The genesis of refractory melts in the formation of
649 oceanic crust. *Contributions to Mineralogy and Petrology* 96, 326-342.

650 Falloon, T.J., Danyushevsky, L.V., 2000. Melting of refractory mantle at 1.5, 2 and 2.5
651 GPa under anhydrous and H₂O-undersaturated conditions: Implications for the
652 petrogenesis of high-Ca boninites and the influence of subduction components
653 on mantle melting. *Journal of Petrology* 41, 257-283.

654 Flower, M.F.J., Levine, H.M., 1987. Petrogenesis of a tholeiite-boninite sequence
655 from Ayios Mamas, Troodos ophiolite: evidence for splitting of a volcanic arc?
656 *Contributions to Mineralogy and Petrology* 97, 509-524.

657 George, R.P., 1978. Structural petrology of the Olympus ultramafic complex in the

658 Troodos ophiolite, Cyprus. Geological Society of America Bulletin 89, 845-865.

659 Golowin, R., Portnyagin, M., Hoernle, K., Sobolev, A., Kuzmin, D., Werner, R., 2017.

660 The role and conditions of second-stage mantle melting in the generation of

661 low-Ti tholeiites and boninites: the case of the Manihiki Plateau and the Troodos

662 ophiolite. Contributions to Mineralogy and Petrology 172, 104.

663 Greenbaum, D., 1972. Magmatic processes at ocean ridges: evidence from the

664 Troodos massif, Cyprus. Nature Physical Science 238, 18-21.

665 Inoue, T., 1994. Effect of water on melting phase relations and melt composition in

666 the system Mg_2SiO_4 - $MgSiO_3$ - H_2O up to 15 GPa. Physics of the Earth and

667 Planetary Interiors 85, 237-263.

668 Irvine, T.N., Smith, C.H., 1967. The ultramafic rocks of the Muskox intrusion,

669 Northwest territories, Canada. Ultramafic and Related Rocks, Wiley, New York,

670 pp. 38-49.

671 Jaques, A.L., Green, D.H., 1980. Anhydrous melting of peridotite at 0–15 kb pressure

672 and the genesis of tholeiitic basalts. Contributions to Mineralogy and Petrology

673 73, 287-310.

674 Jousselein, D., Morales, L.F., Nicolle, M. and Stephant, A., 2012. Gabbro layering

675 induced by simple shear in the Oman ophiolite Moho transition zone. Earth and

676 Planetary Science Letters 331, 55-66.

677 Kamenetsky, V.S., Crawford, A.J., Meffre, S., 2001. Factors controlling chemistry of

678 magmatic spinel: an empirical study of associated olivine, Cr-spinel and melt

679 inclusions from primitive rocks. Journal of Petrology 42, 655-671.

680 Klemme, S., Blundy, J.D., Wood, B.J., 2002. Experimental constraints on major and
681 trace element partitioning during partial melting of eclogite. *Geochimica et*
682 *Cosmochimica Acta* 66, 3109-3123.

683 Kong, J., Niu, Y., Sun, P., Xiao, Y., Guo, P., Hong, D., Zhang, Y., Shao, F., Wang, X.,
684 Duan, M., 2019. The origin and geodynamic significance of the Mesozoic dykes
685 in eastern continental China. *Lithos*.

686 König, S., Münker, C., Schuth, S., Garbe-Schönberg, D., 2008. Mobility of tungsten
687 in subduction zones. *Earth and Planetary Science Letters* 274, 82-92.

688 Konstantinou, A., Wirth, K., Vervoort, J., 2007. U-Pb isotopic dating of Troodos
689 plagiogranite, Cyprus by LA-ICP-MS. *Geological Society of America Abstracts*
690 *with Programs* 39, 388.

691 Kostopoulos, D., Murton, B., 1992. Origin and distribution of components in boninite
692 genesis: significance of the OIB component. *Geological Society, London,*
693 *Special Publications* 60, 133-154.

694 Kushiro, I., 1969. The system forsterite-diopside-silica with and without water at high
695 pressures. *American Journal of Science* 267, 269-294.

696 Laurent, R., 1992. Peridotite intrusions emplaced in the fossil suprasubduction zone
697 environment of Cyprus. *Geological Society, London, Special Publications* 60,
698 233-239.

699 Le Bas, M.J., 2000. IUGS reclassification of the high-Mg and picritic volcanic rocks.
700 *Journal of Petrology* 41, 1467-1470.

701 Li, Y., Kimura, J.I., Machida, S., Ishii, T., Ishiwatari, A., Maruyama, S., Qiu, H.,

702 Ishikawa, T., Kato, Y., Haraguchi, S., Takahata, N., Hirahara, Y., Miyazaki, T.,
703 2013. High-Mg Adakite and Low-Ca Boninite from a Bonin Fore-arc Seamount:
704 Implications for the Reaction between Slab Melts and Depleted Mantle. *Journal*
705 *of Petrology* 54, 1149-1175.

706 Liu, Y., Hu, Z., Gao, S., Günther, D., Xu, J., Gao, C., Chen, H., 2008. In situ analysis
707 of major and trace elements of anhydrous minerals by LA-ICP-MS without
708 applying an internal standard. *Chemical Geology* 257, 34-43.

709 McDade, P., Blundy, J.D., Wood, B.J., 2003. Trace element partitioning between
710 mantle wedge peridotite and hydrous MgO-rich melt. *American Mineralogist* 88,
711 1825-1831.

712 Moores, E.M., Vine, F.J., 1971. The Troodos Massif, Cyprus and other ophiolites as
713 oceanic crust: evaluation and implications. *Philosophical Transactions of the*
714 *Royal Society of London. Series A, Mathematical and Physical Sciences* 268,
715 443-467.

716 Mukasa, S.B., Ludden, J.N., 1987. Uranium-lead isotopic ages of plagiogranites from
717 the Troodos ophiolite, Cyprus, and their tectonic significance. *Geology* 15,
718 825-828.

719 Naslund, H.R., Turner, P.A., Keith, D.W., 1991. Crystallization and layer formation in
720 the middle zone of the Skaergaard Intrusion. *Bulletin of the Geological Society*
721 *of Denmark* 38, 165-171

722 Niu, Y., 1997. Mantle melting and melt extraction processes beneath ocean ridges:
723 Evidence from abyssal peridotites. *Journal of Petrology* 38, 1047-1074.

724 Niu, Y., 2004. Bulk-rock major and trace element compositions of abyssal peridotites:
725 implications for mantle melting, melt extraction and post-melting processes
726 beneath mid-ocean ridges. *Journal of Petrology* 45, 2423-2458.

727 Niu, Y., Waggoner, D.G., Sinton, J.M., Mahoney, J.J., 1996. Mantle source
728 heterogeneity and melting processes beneath seafloor spreading centers: the East
729 Pacific Rise, 18–19°S. *Journal of Geophysical Research: Solid Earth* 101,
730 27711-27733.

731 Niu, Y., Langmuir, C.H., Kinzler, R.J., 1997. The origin of abyssal peridotites: a new
732 perspective. *Earth and Planetary Science Letters* 152, 251-265.

733 O'Hanley, D.S., 1992. Solution to the volume problem in serpentinization. *Geology* 20,
734 705-708.

735 Osozawa, S., Shinjo, R., Lo, C.H., Jahn, B.M., Hoang, N., Sasaki, M., Ishikawa, K.I.,
736 Kano, H., Hoshi, H., Xenophontos, C., Wakabayashi, J., 2012. Geochemistry and
737 geochronology of the Troodos ophiolite: An SSZ ophiolite generated by
738 subduction initiation and an extended episode of ridge subduction? *Lithosphere* 4,
739 497-510.

740 Parkinson, I.J., Pearce, J.A., 1998. Peridotites from the Izu–Bonin–Mariana forearc
741 (ODP Leg 125): evidence for mantle melting and melt–mantle interaction in a
742 supra-subduction zone setting. *Journal of Petrology* 39, 1577-1618.

743 Pearce, J.A., Robinson, P.T., 2010. The Troodos ophiolitic complex probably formed
744 in a subduction initiation, slab edge setting. *Gondwana Research* 18, 60-81.

745 Portnyagin, M., Danyushevsky, L., Kamenetsky, V., 1997. Coexistence of two distinct

746 mantle sources during formation of ophiolites: a case study of primitive
747 pillow-lavas from the lowest part of the volcanic section of the Troodos
748 Ophiolite, Cyprus. *Contributions to Mineralogy and Petrology* 128, 287-301.

749 Presnall, D., Dixon, S.A., Dixon, J.R., O'donnell, T., Brenner, N., Schrock, R., Dycus,
750 D., 1978. Liquidus phase relations on the join diopside-forsterite-anorthite from
751 1 atm to 20 kbar: their bearing on the generation and crystallization of basaltic
752 magma. *Contributions to Mineralogy and Petrology* 66, 203-220.

753 Regelous, M., Haase, K.M., Freund, S., Keith, M., Weinzierl, C.G., Beier, C., Brandl,
754 P.A., Endres, T., Schmidt, H., 2014. Formation of the Troodos Ophiolite at a
755 triple junction: Evidence from trace elements in volcanic glass. *Chemical
756 Geology* 386, 66-79.

757 Resing, J.A., Rubin, K.H., Embley, R.W., Lupton, J.E., Baker, E.T., Dziak, R.P.,
758 Baumberger, T., Lilley, M.D., Huber, J.A., Shank, T.M., Butterfield, D.A.,
759 Clague, D.A., Keller, N.S., Merle, S.G., Buck, N.J., Michael, P.J., Soule, A.,
760 Caress, D.W., Walker, S.L., Davis, R., Cowen, J.P., Reysenbach, A.L., Thomas,
761 H., 2011. Active submarine eruption of boninite in the northeastern Lau Basin.
762 *Nature Geoscience* 4, 799-806.

763 Robinson, P.T., Melson, W.G., O'Hearn, T., Schmincke, H.U., 1983. Volcanic glass
764 compositions of the Troodos ophiolite, Cyprus. *Geology* 11, 400-404.

765 Rollinson, H., 2008. The geochemistry of mantle chromitites from the northern part of
766 the Oman ophiolite: inferred parental melt compositions. *Contributions to
767 Mineralogy and Petrology* 156, 273-288.

768 Saccani, E., Tassinari, R., 2015. The role of MORB and SSZ magma-types in the
769 formation of Jurassic ultramafic cumulates in the Mirdita ophiolites (Albania) as
770 deduced from chromian spinel and olivine chemistry. *Ofioliti* 40, 37-56.

771 Smewing, J.D., Simonian, K.O., Gass, I.G., 1975. Metabasalts from the Troodos
772 Massif, Cyprus: genetic implication deduced from petrography and trace element
773 geochemistry. *Contributions to Mineralogy and Petrology* 51, 49-64.

774 Sobolev, A.V., Chaussidon, M., 1996. H₂O concentrations in primary melts from
775 supra-subduction zones and mid-ocean ridges: implications for H₂O storage and
776 recycling in the mantle. *Earth and Planetary Science Letters* 137, 45-55.

777 Stevens, R.E., 1944. Composition of some chromites of the western hemisphere.
778 *American Mineralogist: Journal of Earth and Planetary Materials* 29, 1-34.

779 Sun, S.S., McDonough, W.F., 1989. Chemical and isotopic systematics of oceanic
780 basalts: implications for mantle composition and processes. Geological Society,
781 London, Special Publications 42, 313-345.

782 Tamura, A., Arai, S., 2006. Harzburgite–dunite–orthopyroxenite suite as a record of
783 supra-subduction zone setting for the Oman ophiolite mantle. *Lithos* 90, 43-56.

784 Taylor, R.N., Nesbitt, R.W., Vidal, P., Harmon, R.S., Auvray, B., Croudace, I.W., 1994.
785 Mineralogy, chemistry, and genesis of the boninite series volcanics, Chichijima,
786 Bonin Islands, Japan. *Journal of Petrology* 35, 577-617.

787 Thy, P., 1987a. Petrogenetic implications of mineral crystallization trends of Troodos
788 cumulates, Cyprus. *Geological Magazine* 124, 1-11.

789 Thy, P., 1987b. Magmas and magma chamber evolution, Troodos ophiolite, Cyprus.

790 Geology 15, 316.

791 Thy, P., Xenophontos, C., 1991. Crystallization orders and phase chemistry of glassy
792 lavas from the pillow sequences, Troodos ophiolite, Cyprus. *Journal of Petrology*
793 32, 403-428.

794 Warren, J.M., 2016. Global variations in abyssal peridotite compositions. *Lithos* 248,
795 193-219.

796 Wasylenki, L.E., Baker, M.B., Kent, A.J., Stolper, E.M., 2003. Near-solidus melting
797 of the shallow upper mantle: partial melting experiments on depleted peridotite.
798 *Journal of Petrology* 44, 1163-1191.

799 Williams, D.W., Kennedy, G.C., 1969. Melting curve of diopside to 50 kilobars.
800 *Journal of Geophysical Research* 74, 4359-4366.

801 Woelki, D., Regelous, M., Haase, K.M., Romer, R.H.W., Beier, C., 2018. Petrogenesis
802 of boninitic lavas from the Troodos Ophiolite, and comparison with
803 Izu–Bonin–Mariana fore-arc crust. *Earth and Planetary Science Letters* 498,
804 203-214.

805 Xiao, Y., Chen, S., Niu, Y., Wang, X., Xue, Q., Wang, G., Gao, Y., Gong, H., Kong, J.,
806 Shao, F., Sun, P., Duan, M., Hong, D., Wang, D., 2020. Mineral compositions of
807 syn-collisional granitoids and their implications for the formation of juvenile
808 continental crust and adakitic magmatism. *Journal of Petrology*, egaa038,
809 <https://doi.org/10.1093/petrology/egaa038>.

1 **Fig. 1.** Simplified geological map of the Troodos Ophiolite (modified from [Batanova](#)
2 [and Sobolev \(2000\)](#) and [Osozawa et al., 2012](#)), showing sample locations (A-C). A:
3 interlayered harzburgite/lherzolite and dunite; B: boninite as pillow lavas from the
4 Arakapas Fault Zone (AFZ); C: boninite as dyke near the AFZ. CY-4 is a bore hole
5 drilled into the lower sheeted dyke complex, gabbros and ultramafic cumulates ([Thy](#)
6 [et al., 1987a](#)). U1 harzburgite and U2 harzburgite are mantle peridotites ([Batanova](#)
7 [and Sobolev, 2000](#)).

8 **Fig. 2.** Field photos of the interlayered ultramafic rocks near the Pano Amiandos and
9 boninites from the Arakapas Fault Zone (AFZ) in the Troodos ophiolite complex. (a, b,
10 c): Interlayered cumulate of serpentinized harzburgite (brown; or lherzolite if locally
11 Cpx rich) and serpentinized dunite (dark grey) with varying thickness on decimeter (a)
12 to millimeter (b) scales. Note that cracks perpendicular to the layering are confined
13 within the harzburgite (a-c). (d, e): Piles of pillow lavas near the AFZ with
14 fresh/altered glassy rinds well preserved. (f): Brownish subvertical boninite dykes
15 cross-cutting basaltic dykes near the AFZ.

16 **Fig. 3.** Photomicrographs of boninite, dunite and harzburgite. (a): Boninite from the
17 AFZ containing phenocrysts of euhedral and subhedral Ol, Opx and Sp, with Ol and
18 pyroxene microlites in the glassy groundmass, very similar to typical boninite from
19 Bonin forearc ([Li et al., 2013](#)) and the modern boninite lava from the Lau Basin
20 ([Resing et al., 2011](#)). (b): Serpentinized dunite from the interlayered cumulate (dark
21 grey layers in Fig. 2a-c). (c, d): Serpentinized harzburgite from the interlayered
22 cumulate (brown layers in Fig. 2a-c). (e, f): Locally Cpx-rich lherzolite from a

23 harzburgite layer of the interlayered cumulate (TDS06-1). Ol, Opx, Cpx, Sp and Srp
24 are olivine, orthopyroxene, clinopyroxene, spinel and serpentine respectively. (a, b, d,
25 f): crossed polarized light; (c, e): plane polarized light.

26 **Fig. 4.** Stitched photomicrographs (left, plane polarized light; right, crossed polarized
27 light) of the interlayered ultramafic cumulate (TDS45-4). The lithology (HZ -
28 harzburgite; DUN - dunite) and mineral (Ol - olivine; Opx - orthopyroxene; Cpx -
29 clinopyroxene) modes (vol. %) of each layer are indicated. These layers can be easily
30 recognized with clear contacts. The harzburgite (HZ) is characterized by cumulate
31 texture and has undergone varying degrees of serpentinization. The dunite is strongly
32 serpentinized. Parallel fractures in the harzburgite (perpendicular to the layering) are
33 filled with serpentines from the adjacent dunite layer, which are in accordance with
34 macroscopic cracks (Fig. 2a-c), resulting from greater volume expansion of dunite
35 during olivine serpentinization. Note the mineral modal heterogeneity on the
36 petrographic scale.

37 **Fig. 5.** N-type MORB (Sun and McDonough, 1989) normalized REE (a) and
38 multielement (b) patterns of the boninite from the Arakapas Fault Zone (AFZ) and the
39 bulk-rock cumulate lherzolite (locally Cpx rich from the harzburgite layer). Fields of
40 boninite glass (Golowin et al., 2017; Woelki et al., 2018) and tholeiite glass from the
41 Akaki Canyon (Regelous et al., 2014) are shown for comparison. There is notable
42 enrichment in fluid soluble elements (e.g., Ba, Rb, U, Sr and Pb) in both samples of
43 boninite near the AFZ and the cumulate lherzolite relative to N-MORB. The boninite
44 near the AFZ has a characteristic U-shape REE pattern, which can be distinguished

45 from the tholeiite glass in Troodos.

46 **Fig. 6.** Histogram of forsterite content for olivine (Fo) from the boninite and the
47 cumulate dunite in the Troodos ophiolite. Olivine from boninite (Golowin et al., 2017)
48 has more variable and higher Fo values than those from the cumulate dunite,
49 indicating that the erupted boninite is more primitive than melt in equilibrium with
50 olivine from the cumulate, which is actually expected (see text). $Fo = 100 \times$
51 $Mg/(Mg+Fe^{2+})$ (total Fe is assumed to be Fe^{2+} in olivine).

52 **Fig. 7.** Mg#-variation diagrams of CaO, FeO, Al_2O_3 and Cr_2O_3 for clinopyroxene
53 from the cumulate harzburgite (HZ)/lherzolite (LZ). Compositions of clinopyroxene
54 from the Troodos mantle peridotite (Batanova and Sobolev, 2000) and the Troodos
55 ultramafic cumulate (UC) near Amiandos (Coogan et al., 2003) are shown for
56 comparison. There are notable differences between Cpx in the mantle peridotite and
57 Cpx in the cumulate HZ/LZ. Cpx from the UC near Amiandos share similar
58 compositions with Cpx from the cumulate HZ/LZ.

59 **Fig. 8.** Compositions of spinel in the cumulate harzburgite/lherzolite and dunite in this
60 study (yellow circle) in the Trivalent Cr-Al- Fe^{3+} ternary cation diagram (a) and Cr# vs.
61 Mg# diagram (b). Compositions of spinel in Troodos boninite glasses from the
62 literature (Golowin et al., 2017; Woelki et al., 2018) are shown for comparison (red
63 cross). The spinel compositional fields for boninites and ophiolite chromitites in (a)
64 are from Barnes and Roeder (2001). Fields for boninites and forearc peridotite in (b)
65 are modified from Tamura and Arai (2006) and Parkinson and Pearce (1998). Data of
66 spinel compositions in abyssal peridotites are from Warren (2016). The dashed lines

67 in (b) is the original boninite fields which is updated with solid lines based on the data
68 in this study. The compositions of spinel in the cumulate harzburgite/lherzolite and
69 dunite are close to those in boninite and lie in the field of ophiolite chromitites and
70 forearc peridotites.

71 **Fig. 9.** Comparison of the calculated parental melt compositions (TiO_2 vs. Al_2O_3) in
72 equilibrium with spinel of the studied ultramafic cumulate, boninite glass (Woelki et
73 al., 2018) and tholeiite glasses in Troodos (Pearce and Robinson, 2010). The
74 compositional fields of boninite, island arc tholeiitic (IAT) and MORB are drawn for
75 comparison (modified from Allahyari et al. (2014) and Saccani and Tassinari (2015)).
76 The calculated melts are characteristic of boninite in this well-studied major element
77 compositional space.

78 **Fig. 10.** N-MORB normalized incompatible element abundances of average
79 clinopyroxene (Cpx) and orthopyroxene (Opx) in the cumulate harzburgite/lherzolite,
80 calculated melts in equilibrium with the Cpx and Opx and boninite in this study.
81 Fields for the boninite glass (Golowin et al., 2017; Woelki et al., 2018) and tholeiite
82 glasses (Regelous et al., 2014) from the Troodos ophiolite are shown for comparison.
83 The calculated melts in equilibrium with Cpx and Opx in the cumulate share the same
84 trace element systematics as the Troodos boninite, pointing to their genetic link.
85 Relative standard deviation (RSD) of REE for Cpx is within 20% except for La, Ce,
86 Pr, Nd and Sm (within 30%). RSD of REE for Opx is higher (> 30 % for La, Ce, Pr,
87 Nd, Sm, Eu, Gd and Tb) due to the lower concentrations, but the effect of this
88 fluctuation on the melt calculated from Opx is within the boninite glass field.

89 **Fig. 11.** The Troodos boninite glass compositions in SiO₂, Al₂O₃ and CaO vs. MgO
90 spaces (Golowin et al., 2017; Woelki et al., 2018) can be modeled to be consistent
91 with liquid lines of descent using Petrolog 3.1.1.3 (Danyushevsky and Plechov, 2011).
92 The start composition is the primary magma used by Golowin et al. (2017) from
93 boninite in Troodos (Mg# = 0.78) (Supplementary Table S9). The liquidus phases
94 crystallized can readily explain the layered ultramafic cumulate we study. Under 0.1
95 GPa with a crystallization order of Ol→Opx→Cpx, the cumulate dunite, harzburgite
96 and lherzolite can be produced, respectively, after 1 ~ 14 %, 15 ~ 24 % and 25 ~ 29 %
97 fractional crystallization (see Supplementary Table S10). Thus, the observations and
98 modelling all support the hypothesis that the cumulate dunite-harzburgite/lherzolite
99 result from boninite magma evolution.

100 **Fig. 12.** Simplified Forsterite (Fo)-Enstatite (En)-Diopside (Di) ternary phase
101 diagrams to approximate the natural Ol-Opx-Cpx phase relationships to illustrate the
102 petrogenesis of the interlayered dunite and harzburgite/lherzolite cumulate in the
103 Troodos ophiolite. The dashed lines are isotherms at intervals of 100 °C and the solid
104 lines are cotectic lines. The melting temperatures for Fo, En, Di are from Davis and
105 England (1964), Boyed et al. (1964), Williams and Kennedy (1969). The eutectic
106 temperatures of Di-En, Fo-Di and Fo-En joins at 2 GPa are from Kushiro (1969),
107 Presnall et al. (1978) and Inoue (1994) respectively. Note that the natural water
108 saturated Ol-Opx-Cpx systems appropriate for boninite magmatism necessarily have
109 lower temperatures than these dry Fo-En-Di systems, but the concept and process we
110 show are valid demonstrations. The parental melt begins to crystallize olivine to form

111 a dunite layer before reaching the Ol-Opx cotectic (A→B), along which Ol and Opx
112 coprecipitate to form a harzburgite layer (C→D). The melt will evolve to the
113 Ol-Opx-Cpx eutectic (E) to form harzburgite with some Cpx or lherzolite if the
114 replenishment is delayed. Periodical melt injection into the magma chamber results in
115 dunite-harzburgite interlayered cumulate, in cycles of a→b→c→(d)
116 →a→b→c→(d)... L, liquid; DUN, dunite; HZ, harzburgite; LZ, lherzolite.

117 **Fig. 13.** Schematic illustration showing the formation of the interlayered dunite (DUN)
118 and harzburgite (HZ)/lherzolite (LZ) cumulate. The cumulate sequence is best
119 understood as the result of fractional crystallization of periodically replenished
120 mantle-derived boninite melts as illustrated in terms of phase equilibria (Fig. 12) and
121 schematically in (a). (b-f) illustrate the development of the cumulate. After the
122 formation of a dunite-harzburgite/lherzolite sequence in a magma chamber (b, Fig.
123 11), primitive melt (Mg#₁) with high temperature injects into the magma chamber (c).
124 The erupted melt (Mg#₂) consists of much of the newly replenished primitive melt
125 having Mg#₁ mixed with the existing prior evolved melt. The unerupted melt mixing
126 with the evolved melt in the magma chamber (Mg#₃) continue the crystallization to
127 form next cumulate layers (c-e, f). That is, the interlayered cumulate forms as
128 resulting from periodically replenished (injected) and periodically erupted steady-state
129 open magma chamber system. The varying thickness of the layers (see Fig. 2a-c)
130 reflects varying frequency and varying volume of melt supply pulses.

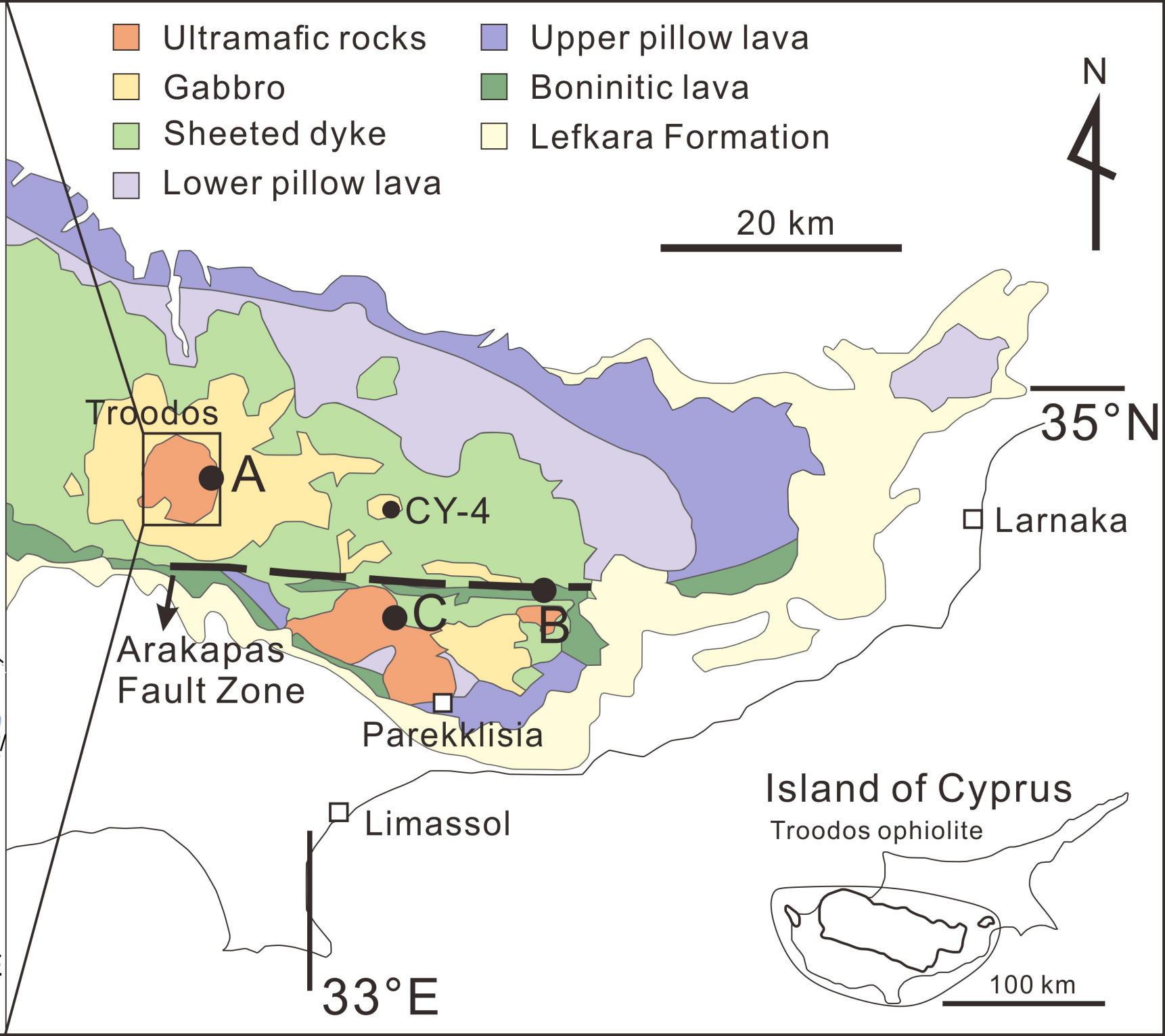
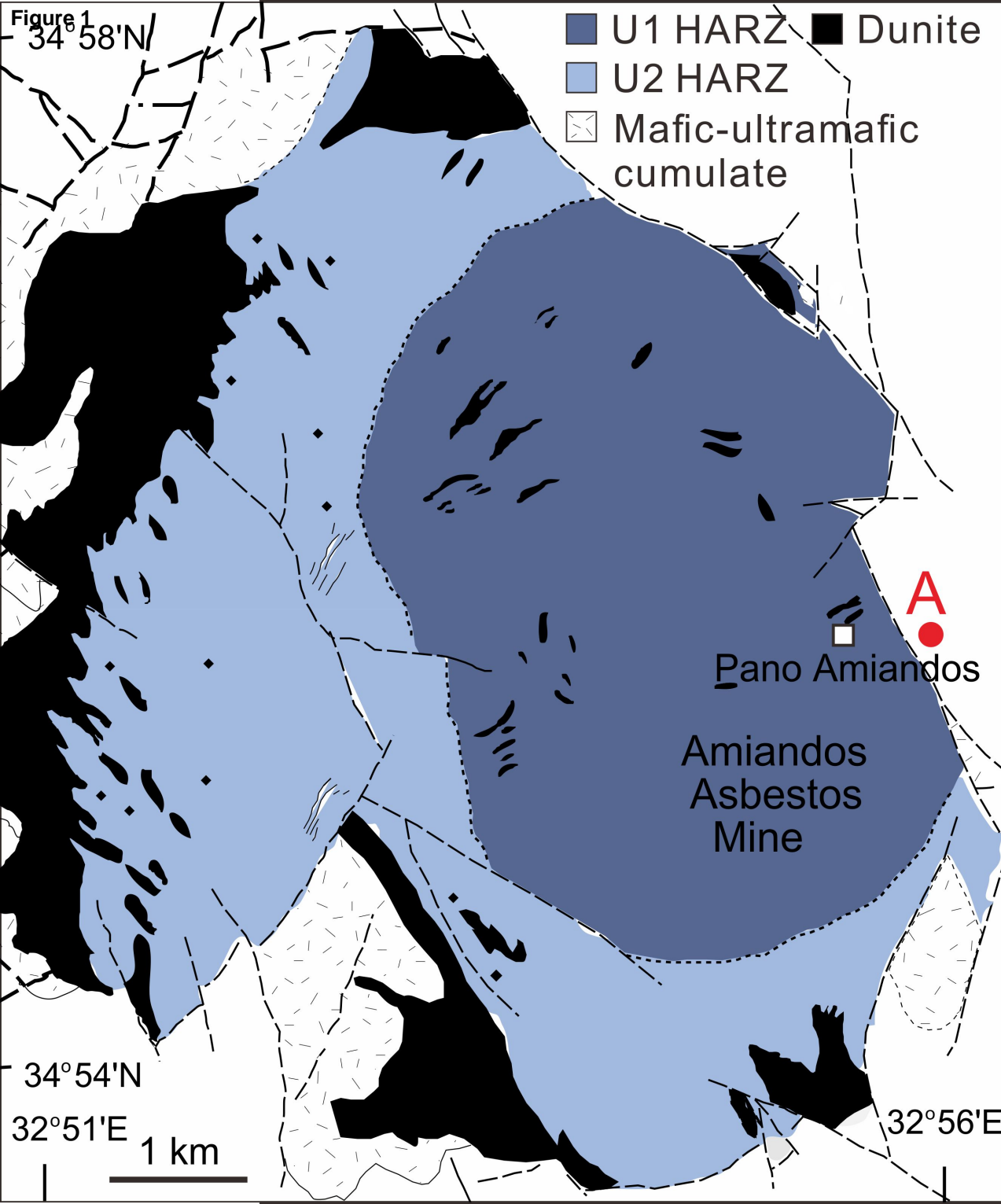
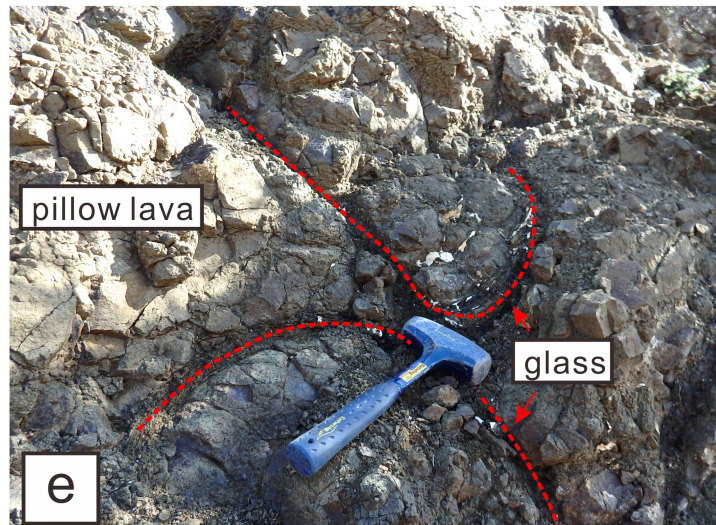


Figure 2



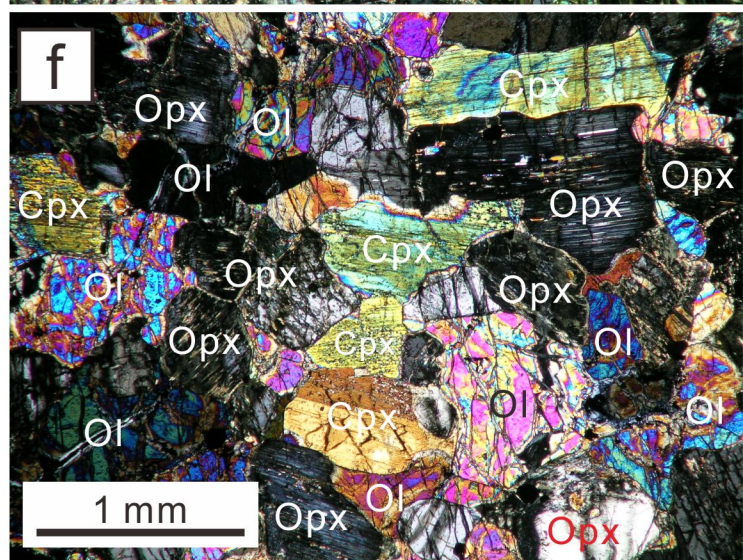
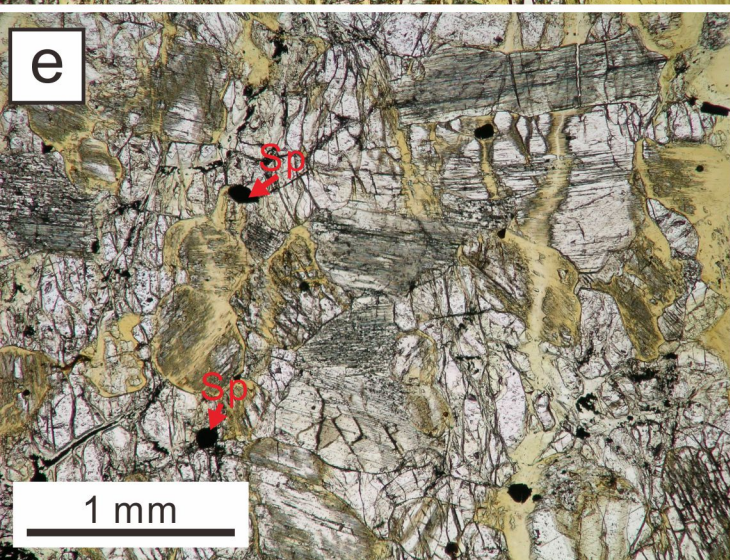
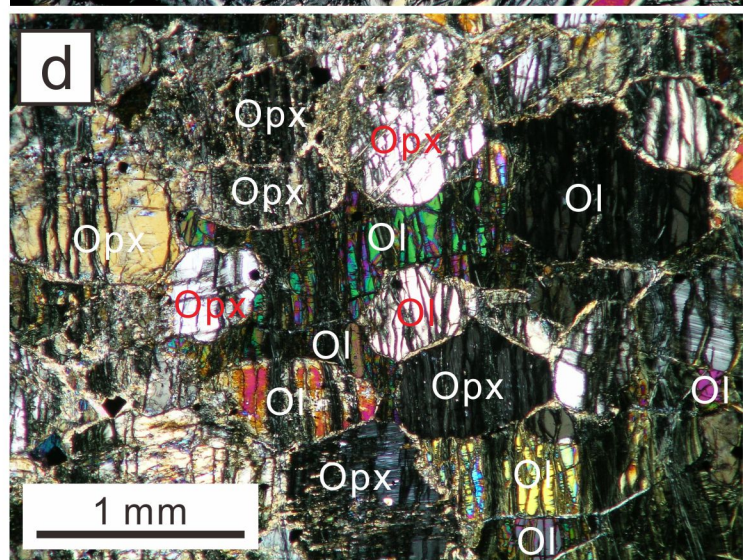
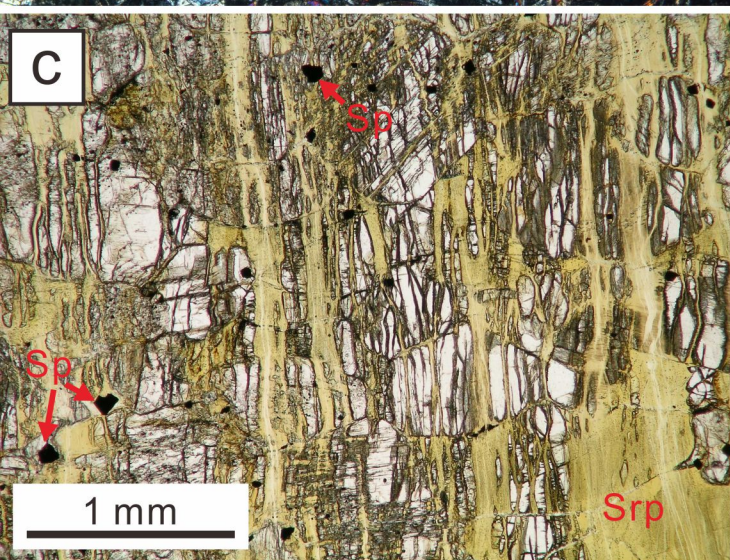
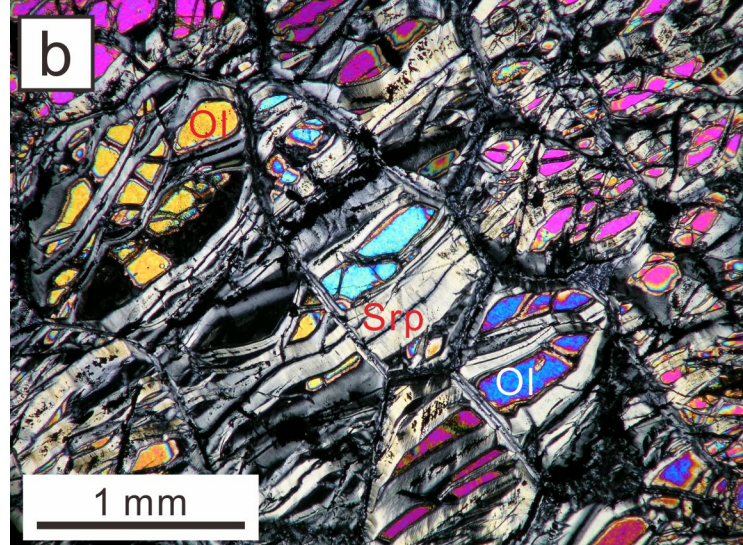
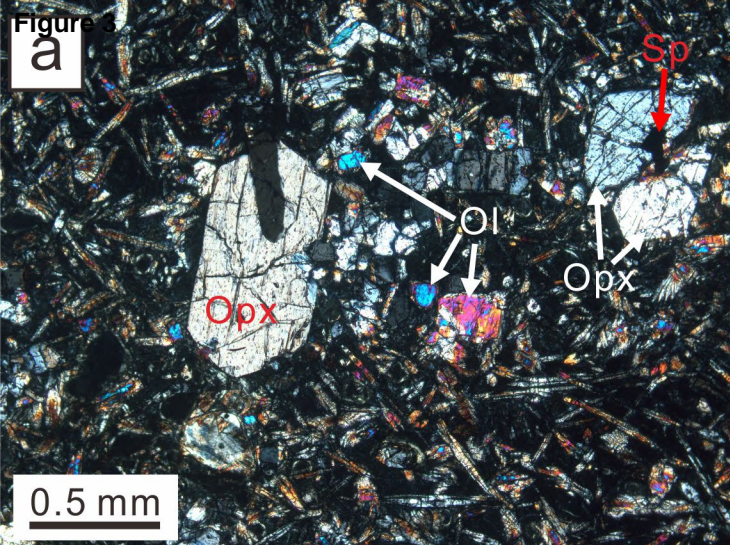
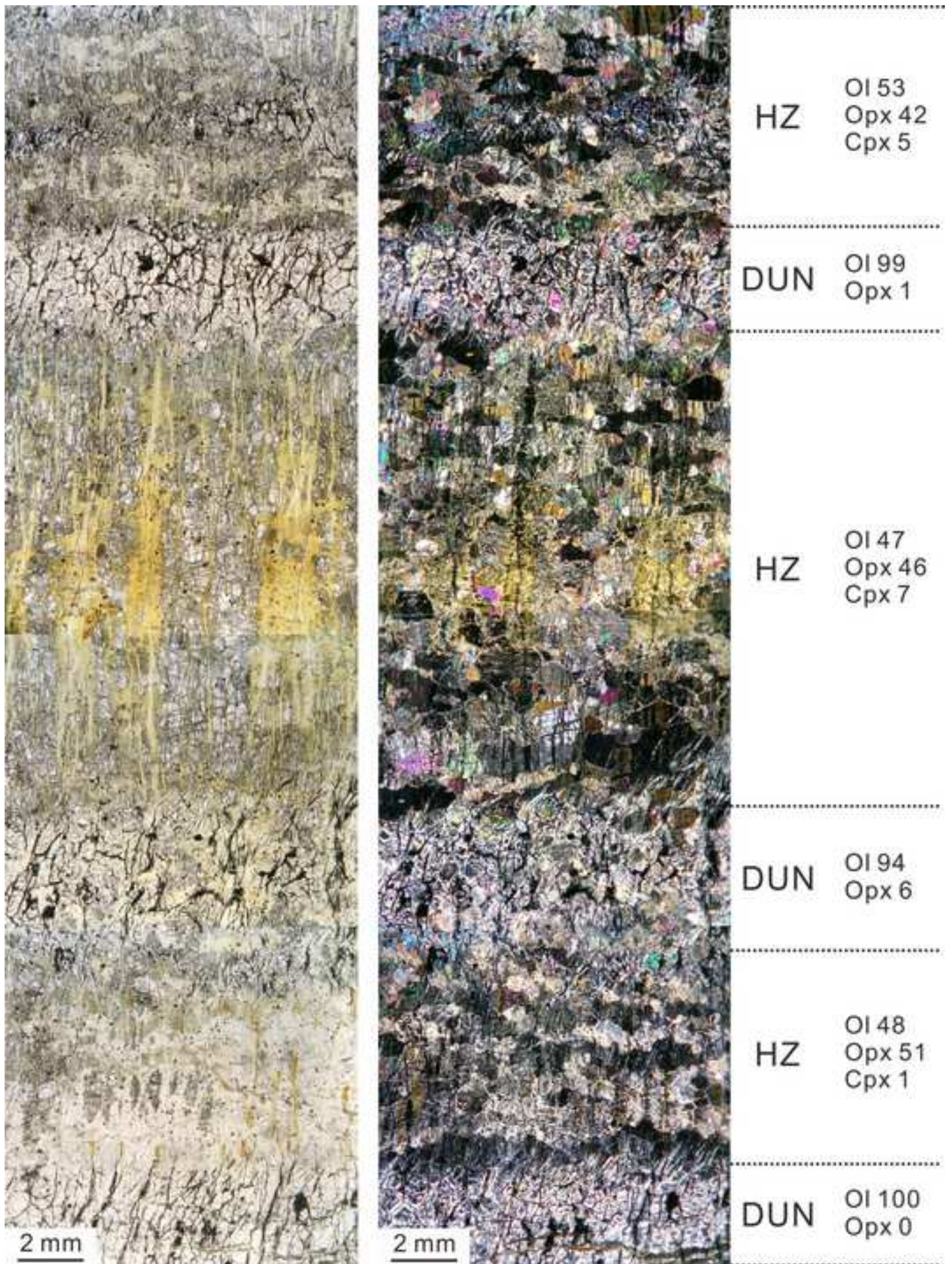


Figure 4
[Click here to download high resolution image](#)



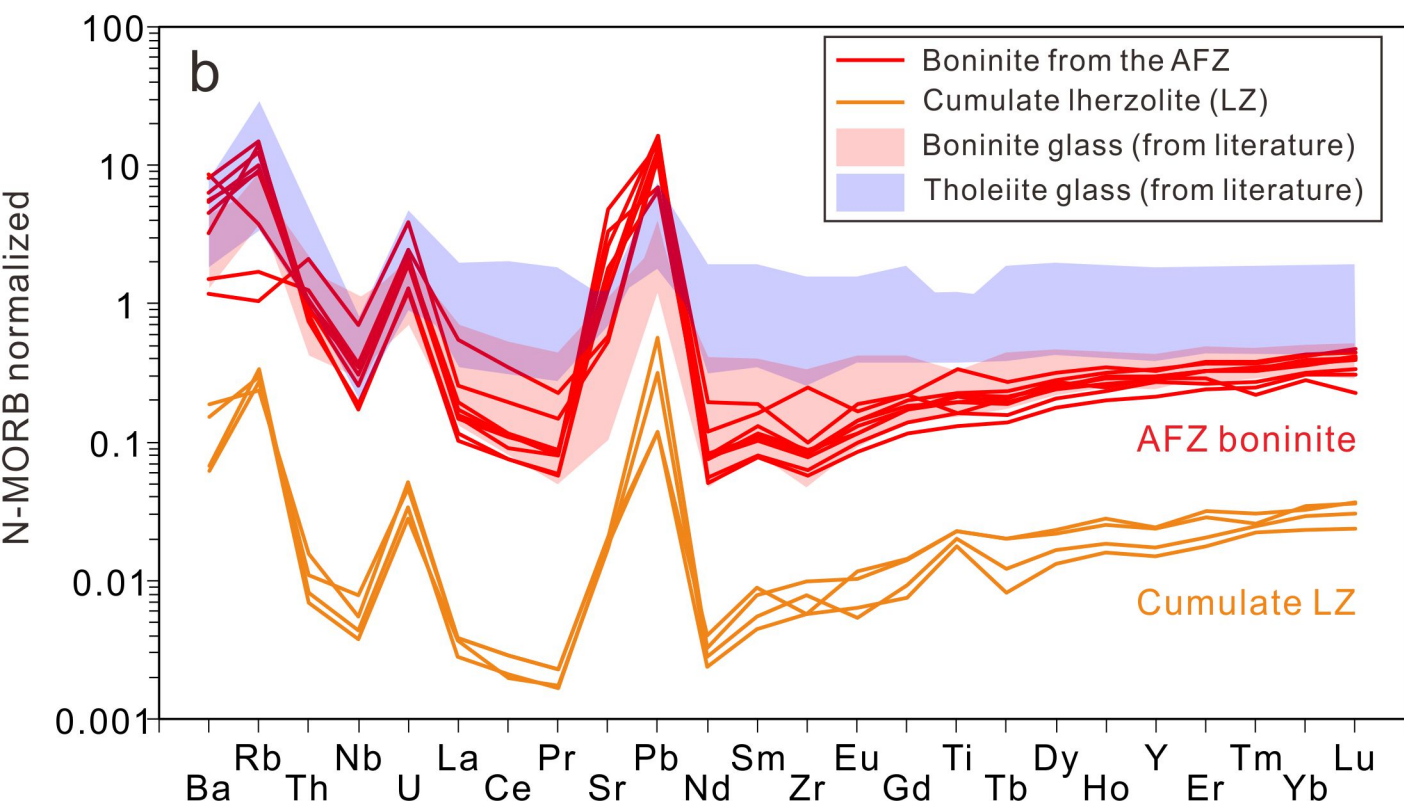
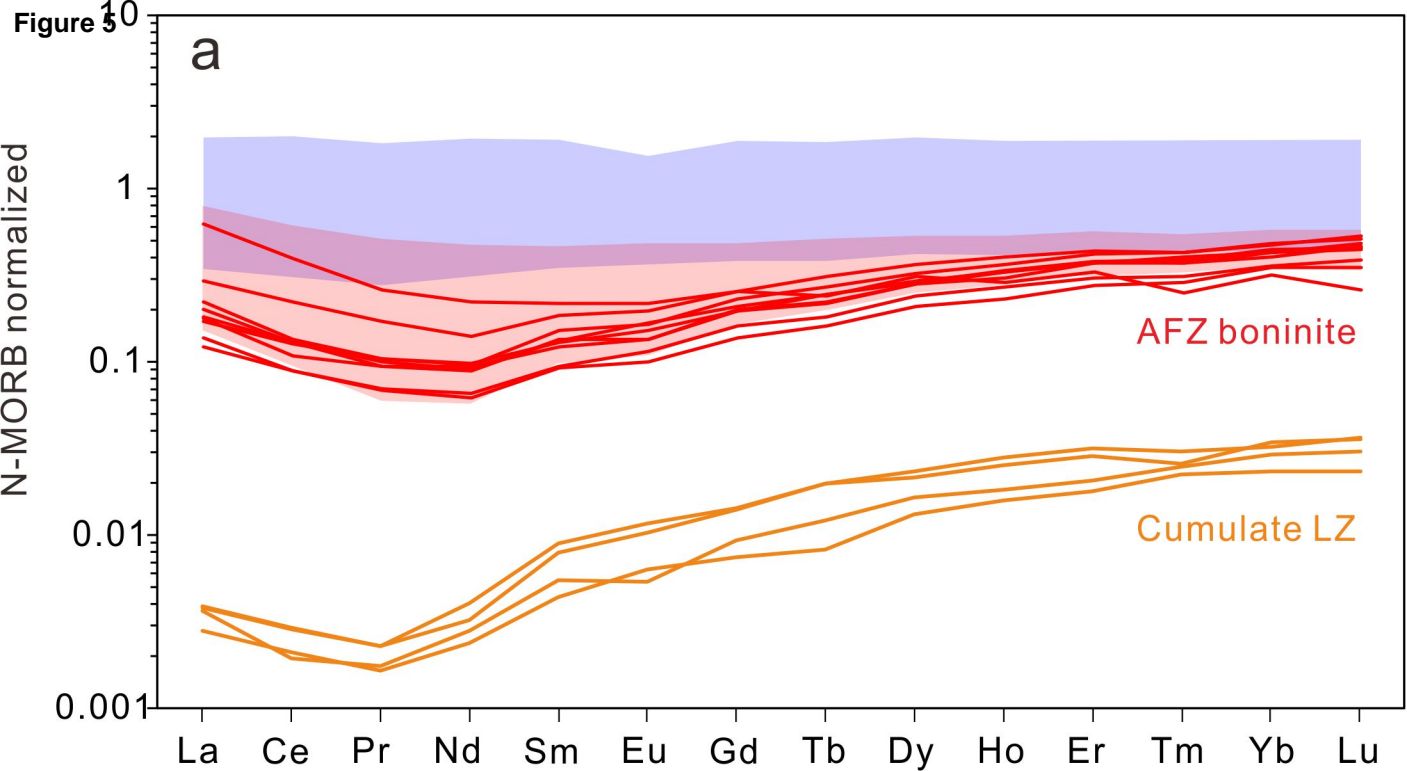
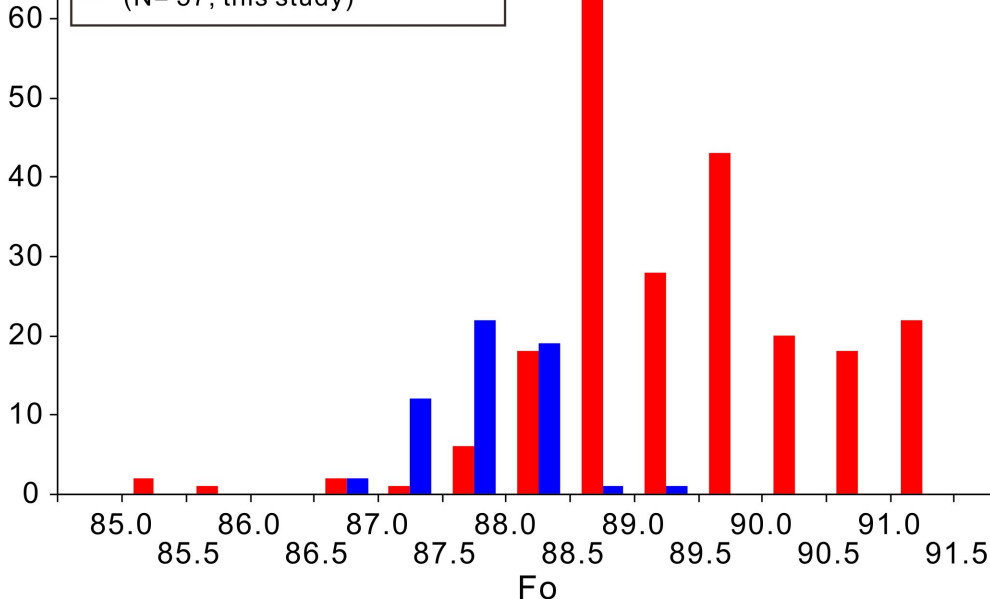


Figure 6

Frequency

■ Ol from boninite glass
(N=229, Golowin et al., 2017)

■ Ol from cumulate dunite
(N= 57, this study)



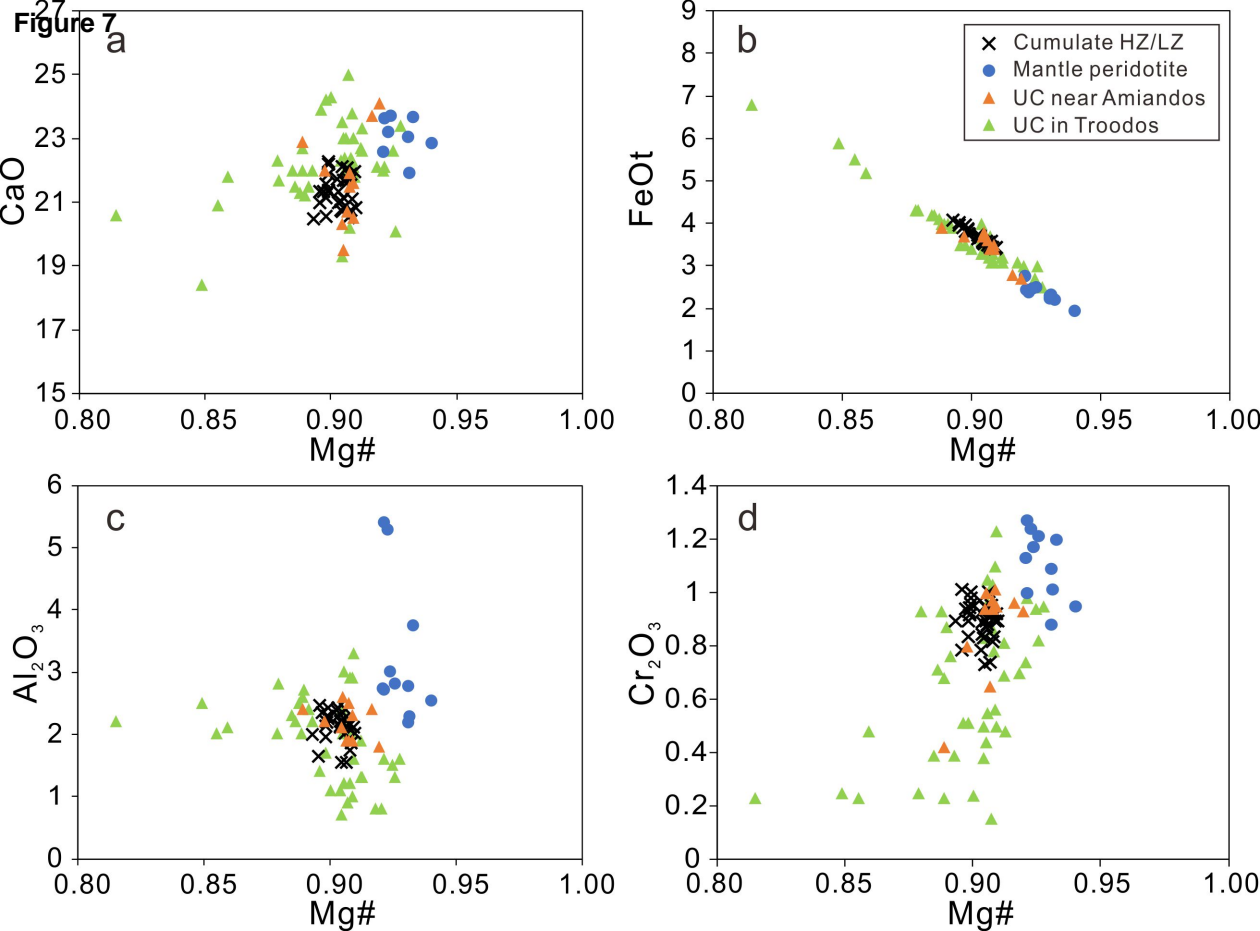
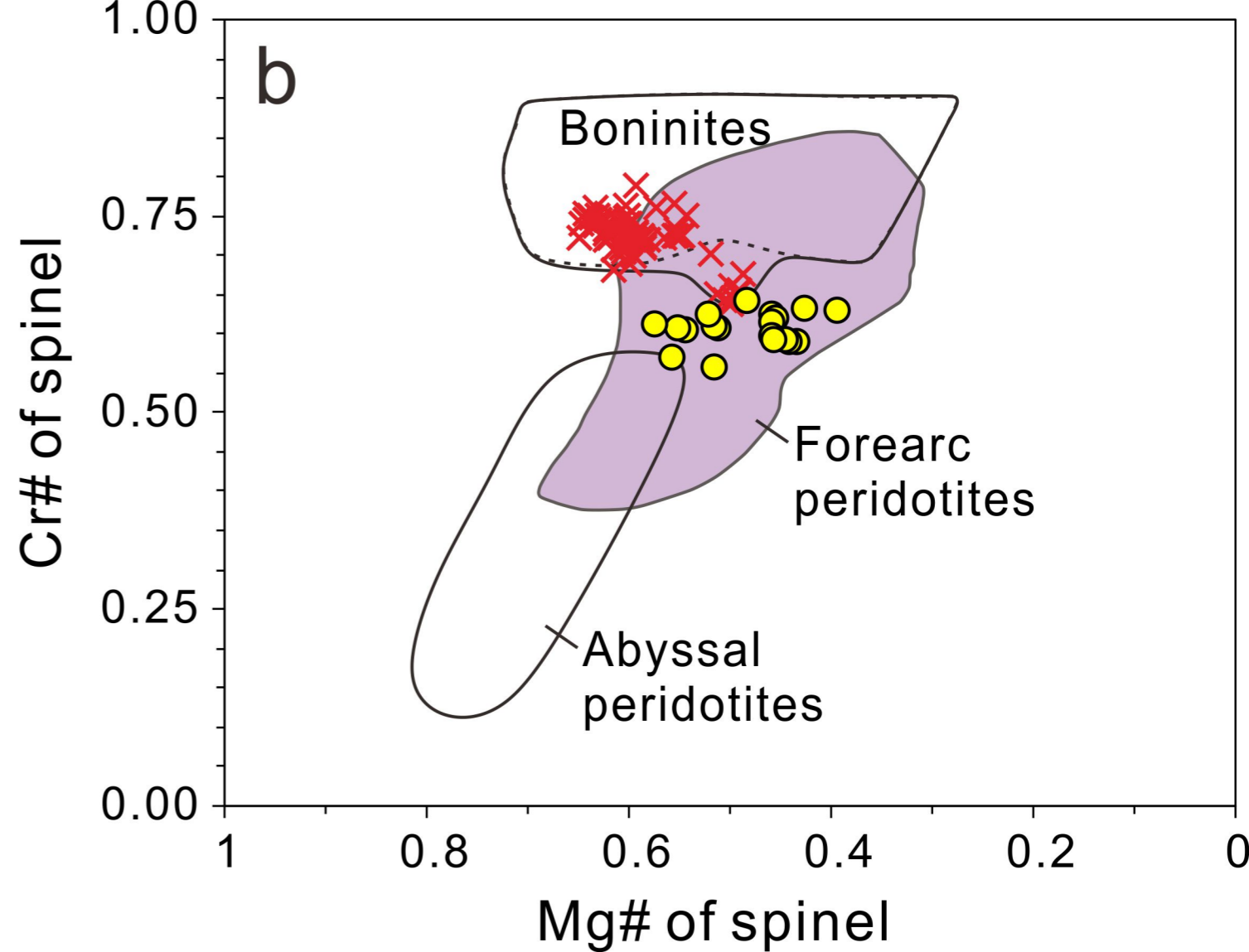
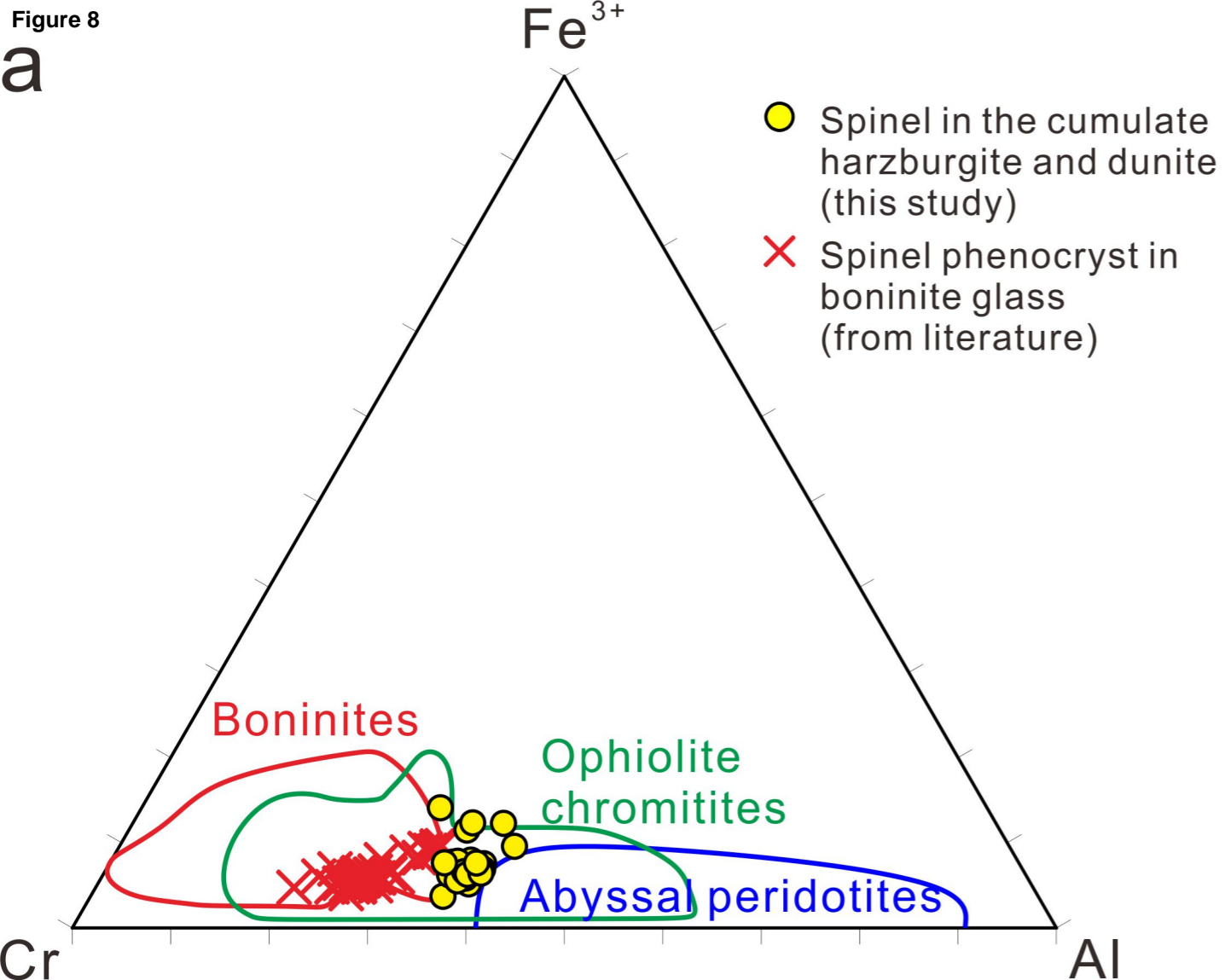
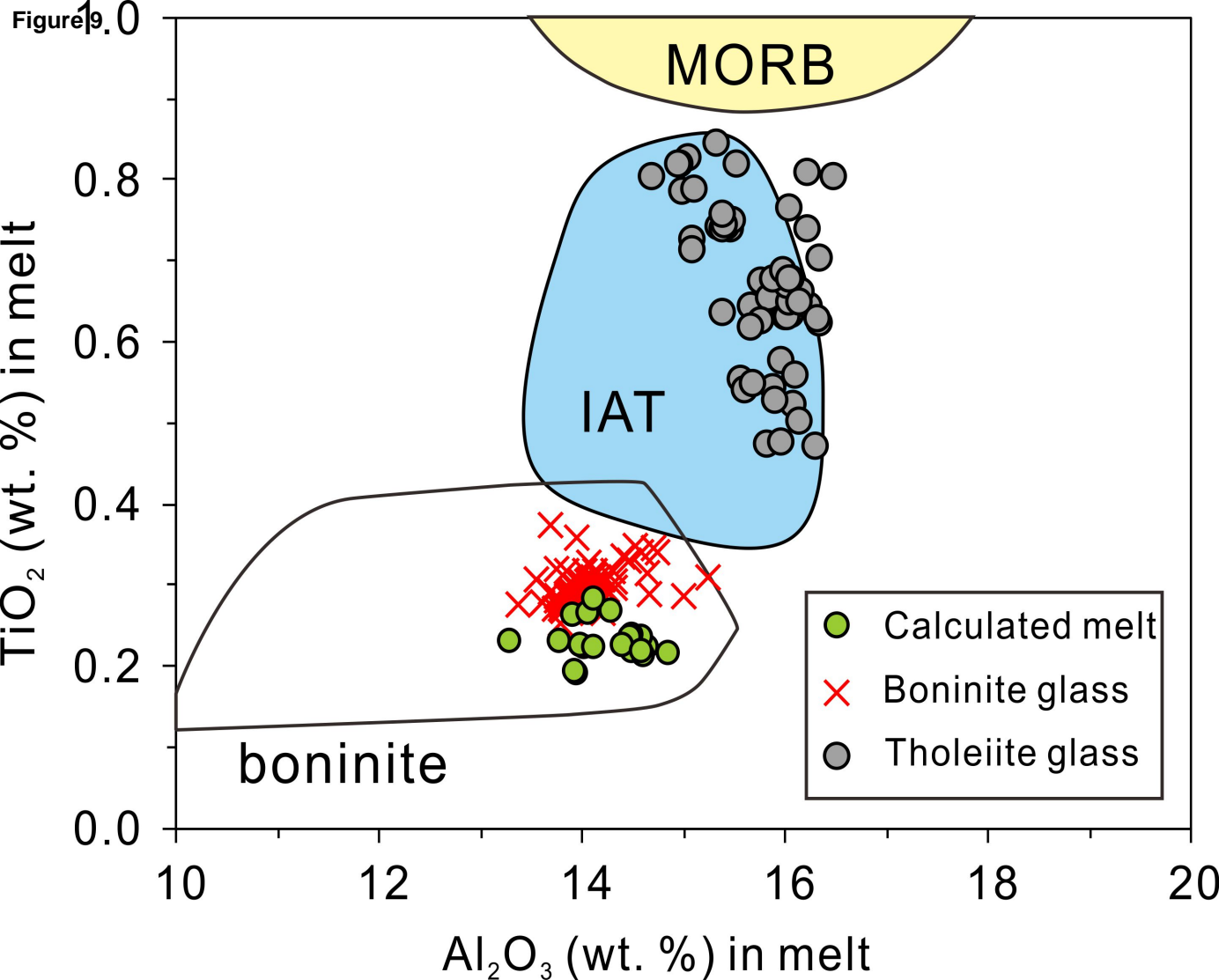
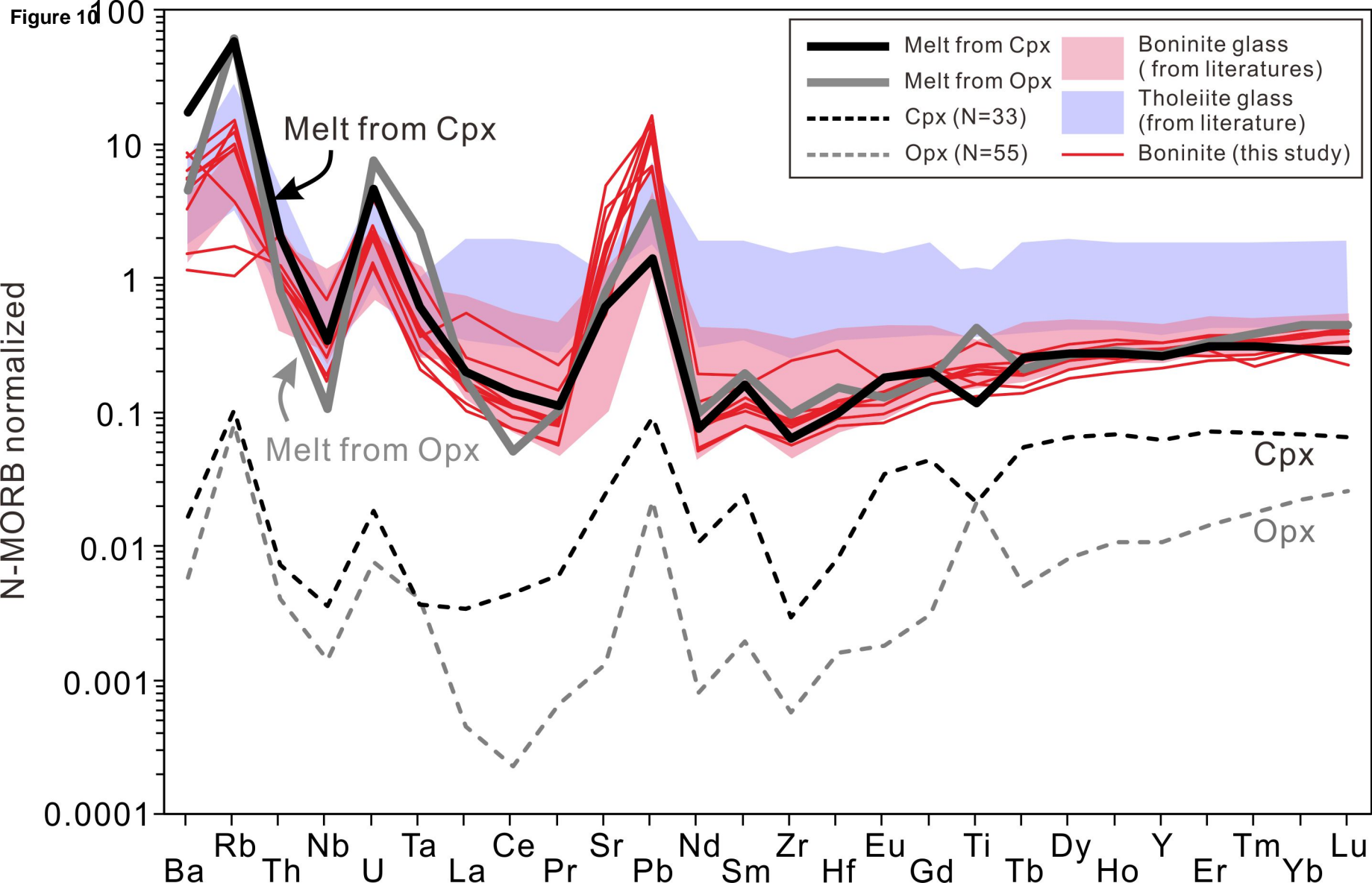


Figure 8

a







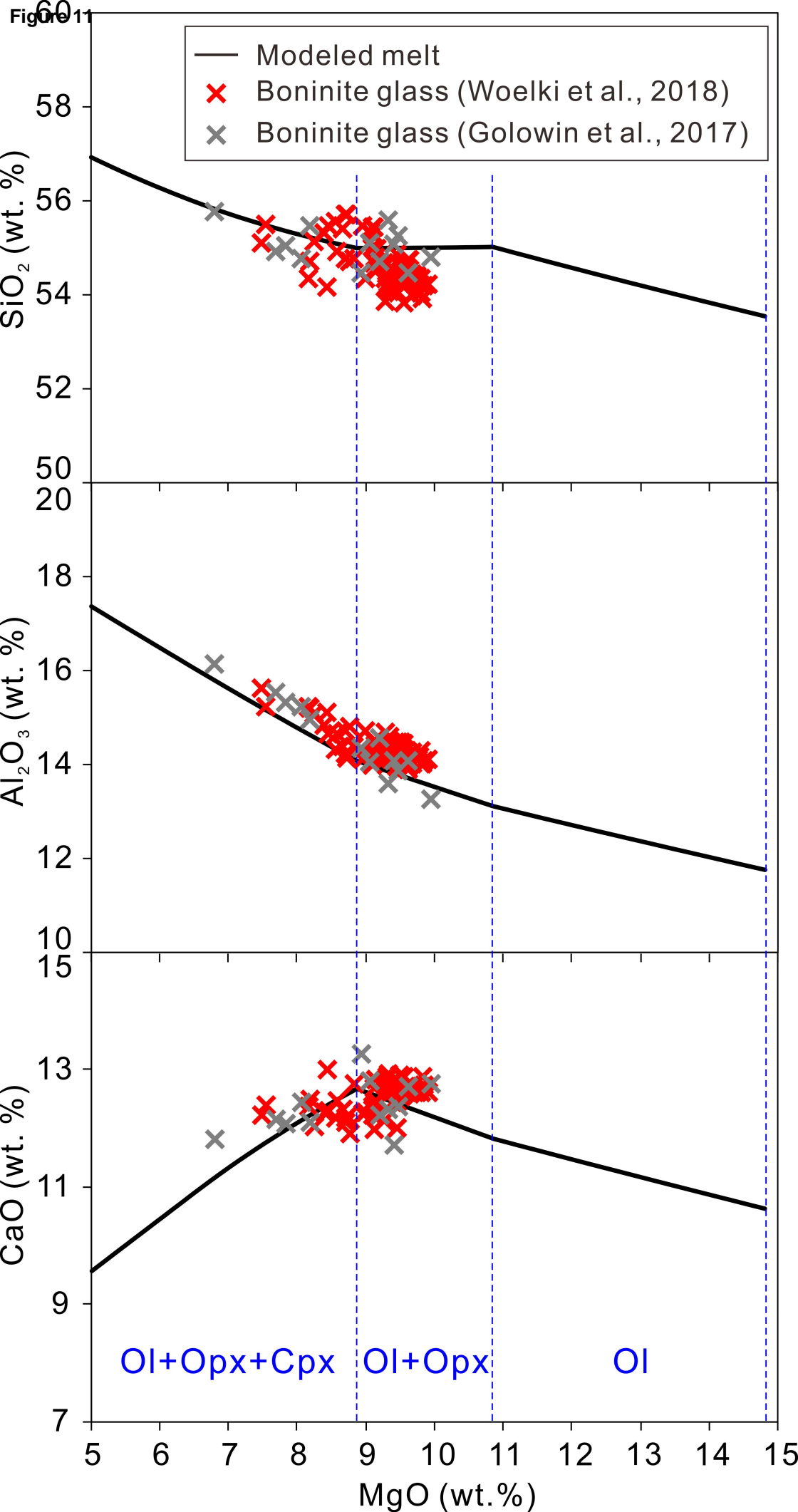


Figure 12

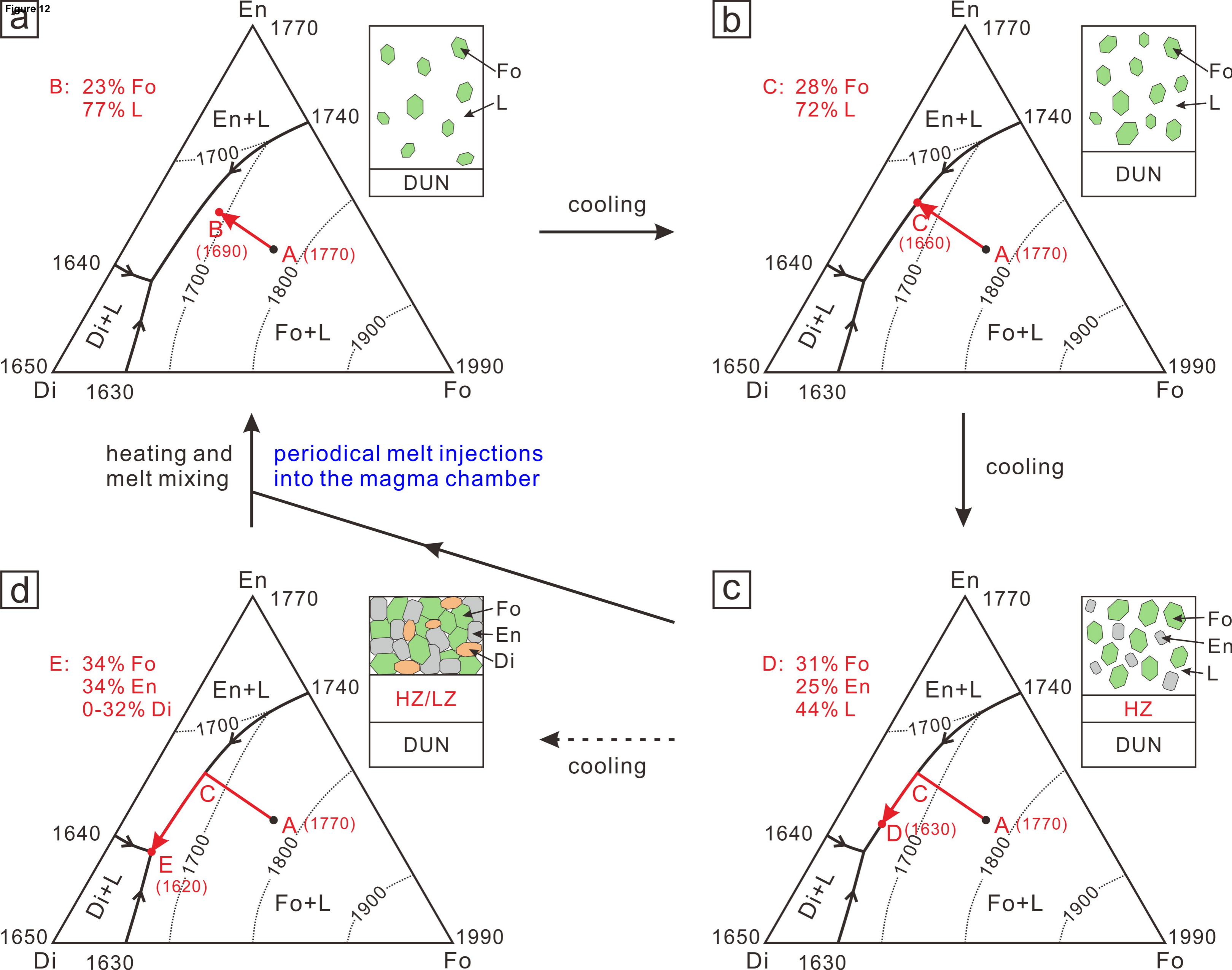


Figure 13

